remote sensing

MDPI

Article

Conditional Evaluation of FY-3E WindRAD Data and ERA5 Reanalysis Fusion for Short-Term Typhoon Wind Vector Prediction

Jun Liu [1], Jie Cui [1] and Yan Liu [2,*]

[1] School of Computer, Electronics and Information, Guangxi University, Nanning 530004, China; liujun@gxu.edu.cn (J.L.); 2313593003@st.gxu.edu.cn (J.C.)
[2] State Key Laboratory of Severe Weather Meteorological Science and Technology, China Meteorology Administration Earth System Modeling and Prediction Centre, Beijing 100081, China
* Correspondence: liuyan@cma.gov.cn

Highlights

What are the main findings?

- FY-3E fusion shows conditional numerical benefits that depend on coverage, band, temporal matching, and sample composition.
- Under the band-specific setting, Ku-band gated fusion shows the clearest numerical improvement, while the ±3 h window provides the best balance between sample availability and temporal consistency.

What are the implications of the main findings?

- FY-3E observations should be integrated with explicit consideration of observation coverage and temporal matching rather than assumed to improve ERA5-based prediction universally.
- Larger multi-year datasets and storm-level validation are needed before drawing operational conclusions about preferred bands or fusion architectures.

Abstract

Typhoon wind prediction is important for disaster prevention. ERA5 reanalysis provides spatially continuous wind fields but may smooth local structures, whereas FY-3E WindRAD, a dual-frequency scatterometer, observes ocean surface winds through C-band and Ku-band measurements with sparse coverage and temporal mismatch. This study evaluates the conditional value of fusing FY-3E WindRAD data with ERA5 for 12-h short-term typhoon wind vector prediction using matched 2023 samples. We compared ERA5-only, naive, mask-aware, and gated fusion across coverage-sensitivity, band-comparison, and temporal-window experiments. Results show that FY-3E fusion provides conditional numerical benefits rather than consistent improvements. Under the band-specific evaluation, Ku-band gated fusion reduced vector root mean square error (RMSE) from 5.736 to 5.366 m/s and average wind speed error (AWSE) from 3.597 to 3.276 m/s, although these improvements were not statistically significant after multiple-comparison correction. Dual-band gated fusion did not outperform the ERA5-only baseline, and under the common-sample evaluation neither Ku-band nor Dual-band showed a clear advantage. The ±3 h window provided a more favorable balance between sample availability and temporal consistency than the wider ±6 h window. Overall, FY-3E WindRAD data provides complementary information, but its effectiveness depends on coverage, band selection, temporal matching, and fusion strategy.

Check for updates

Academic Editor: Weimin Huang

Received: 24 July 2026
Revised: 9 October 2026
Accepted: 18 October 2026
Published: 26 October 2026

Copyright: © 2026 by the authors. Licensee MDPI, Basel, Switzerland. This article is an open access article distributed under the terms and conditions of the Creative Commons Attribution (CC BY) license.

Keywords: conditional evaluation; typhoon wind vector prediction; data fusion; FY-3E WindRAD; ERA5 reanalysis; scatterometer

1. Introduction

Typhoons, a type of tropical cyclone (TC), occur primarily over the northwestern Pacific Ocean and are characterized by high frequency, strong destructive potential, and wide spatial influence. Each year, typhoons pose a serious threat to coastal regions, socio-economic activities, and public safety in China and neighboring countries [1,2]. Among the various physical factors associated with typhoon hazards, the spatial distribution and temporal evolution of near-surface wind fields are particularly important, because they directly determine wind-related damage, marine hazards, and emergency response requirements [3,4].

Traditional typhoon wind field prediction relies heavily on numerical weather prediction (NWP) models, such as the Weather Research and Forecasting (WRF) model. Although NWP models provide strong physical interpretability, their forecast accuracy can be affected by initial condition uncertainty, parameterization errors, and high computational cost [5,6]. In recent years, deep learning has provided an alternative approach for meteorological prediction. Convolutional neural networks (CNNs) have been widely used to extract spatial structures from gridded meteorological fields, while recurrent and spatiotemporal models such as LSTM and ConvLSTM have been applied to model temporal evolution in weather systems [7–9]. These methods have demonstrated potential for short-term wind field prediction.

ERA5 reanalysis is commonly used in deep learning-based wind prediction because it provides spatially continuous and physically consistent gridded fields. However, reanalysis products are model-based assimilated datasets, and local wind structures in rapidly evolving typhoon systems may be smoothed. Satellite scatterometers provide observation-based ocean surface wind information and can offer complementary spatial and retrieval characteristics relative to reanalysis data. FY-3E WindRAD is a dual-frequency scatterometer capable of observing ocean surface winds through C-band and Ku-band measurements [10–12]. Prior to FY-3E, the HY-2C scatterometer provided similar sea surface wind products that have been validated against buoy observations [13]. FY-3E WindRAD adopts a similar rotating fan-beam design to the CFOSAT scatterometer [14], providing high-resolution wind measurements over the ocean. These observations are potentially useful for improving typhoon wind field prediction, especially over ocean regions where in-situ observations are limited. Previous studies have validated the accuracy of WindRAD wind products against buoy observations and other scatterometer products, demonstrating its capability for typhoon monitoring [15–17]. Beyond product validation, ref. [18] demonstrated that FY-3E WindRAD measurements alone can provide accurate tropical cyclone center estimates in the dawn-dusk orbit, highlighting the potential of WindRAD for typhoon monitoring; more broadly, scatterometer winds have been widely assimilated into operational NWP systems to improve typhoon forecasts. Refs. [19,20] demonstrated that ASCAT scatterometer winds improve global forecast system performance through careful quality control and thinning. Ref. [21] further showed that the impact of scatterometer winds in the ECMWF system is sensitive to observation error specifications. In the typhoon-specific context, refs. [22,23] reported positive impacts from assimilating QuikSCAT and CFOSAT scatterometer winds, respectively, into regional typhoon forecast models. These studies consistently indicate that scatterometer observations can improve typhoon wind field analysis, but their effectiveness depends on data quality control, rain contamination handling, and assimilation

strategies—findings that motivate our conditional evaluation of FY-3E WindRAD fusion for deep learning-based typhoon prediction.

However, directly using FY-3E WindRAD observations in deep learning models remains challenging. First, satellite scatterometer data are swath-dependent and spatially incomplete, so the observed region may cover only part of the storm-centered prediction patch. Second, FY-3E overpasses are temporally intermittent, and the observation time may not exactly match the target typhoon sample. Third, different FY-3E bands may have different retrieval characteristics, and their contribution to prediction performance may vary across evaluation metrics. Therefore, it is necessary to evaluate not only whether FY-3E observations are useful, but also under what coverage, band, temporal matching window, and fusion strategy they can provide complementary information.

Despite the demonstrated potential of deep learning for typhoon wind prediction, and the availability of FY-3E WindRAD scatterometer observations, several critical questions remain unresolved. First, while previous studies have validated the accuracy of WindRAD wind products against buoys and other scatterometers [15–17], it is unclear whether these observations actually improve predictive performance when fused with reanalysis data, rather than merely serving as an external observational reference. Second, existing fusion approaches typically assume that adding satellite channels automatically enhances model accuracy, yet the sparse, swath-dependent, and temporally intermittent nature of scatterometer data suggests that this benefit may be conditional rather than guaranteed. Third, no systematic evaluation has been conducted to determine how spatial coverage, frequency band (C-band vs. Ku-band vs. Dual-band), temporal matching window, and fusion strategy collectively influence the effectiveness of satellite–reanalysis integration for typhoon wind vector prediction.

To address these gaps, this study aims to empirically evaluate the conditions under which FY-3E WindRAD scatterometer data provide complementary information to ERA5 reanalysis for short-term typhoon wind vector prediction. The main contributions of this study are fourfold:

1. Conditional evaluation of observation coverage. Under the evaluated C-band settings, the lowest coverage threshold (coverage ≥ 0.10) did not outperform the ERA5-only baseline, whereas the intermediate threshold (coverage ≥ 0.20) provided a more favorable balance between satellite observation availability and sample retention.

2. Quantification of band-dependent performance. In the band-specific experiments, Ku-band gated fusion showed the clearest numerical improvement, reducing Vector_RMSE from 5.736 to 5.366 m/s, although the improvement was not statistically significant after multiple-comparison correction. Dual-band gated fusion did not outperform the ERA5-only baseline.

3. Evaluation of temporal matching sensitivity. The ± 3 h window provided a more favorable balance between sample availability and temporal consistency, whereas the wider ± 6 h window did not yield consistent fusion gains.

4. Methodological insight from controlled comparisons. The common-sample evaluation (N = 179) showed that band-specific performance rankings depend on sample composition: after controlling the sample set, Ku-band performance was approximately comparable to ERA5-only, while Dual-band did not show an advantage. This highlights the importance of controlled sample composition in small-sample satellite–reanalysis fusion studies.

The novelty of this study lies not in proposing a complex new forecasting model, but in rigorously testing the assumption that scatterometer observations automatically improve reanalysis-based prediction. By systematically varying coverage, band, temporal window, and fusion strategy, we provide empirical evidence on when—and when not—FY-3E

observations are valuable. This conditional evaluation framework provides methodological guidance for future satellite–reanalysis fusion studies and potential forecasting applications.

The remainder of this paper is organized as follows. Section 2 describes the data sources, FY-3E preprocessing, multimodal sample construction, model architectures, and experimental setup. Section 3 reports the experimental results, including coverage sensitivity, band comparison, common-sample evaluation, temporal-window sensitivity, benchmark comparisons, and Group cross-validation. Section 4 discusses the physical interpretation of the results, their relation to prior work, and the limitations of this study. Section 5 concludes the paper.

2. Materials and Methods

2.1. Data Sources and Study Area

Typhoon track data were obtained from the Best Track Dataset of Tropical Cyclones released by the China Meteorological Administration (CMA). The dataset provides typhoon center position, maximum wind speed, and minimum central pressure at 6-h intervals. These records were used to identify typhoon samples and determine storm-centered spatial patches.

ERA5 reanalysis wind fields were obtained from the European Centre for Medium-Range Weather Forecasts (ECMWF) as the ERA5 hourly data on single levels (product identifier: 'reanalysis-era5-single-levels'), accessed through the Copernicus Climate Data Store. ERA5 is the fifth generation ECMWF reanalysis, providing hourly global estimates of atmospheric, ocean-wave, and land-surface variables. In this study, ERA5 wind components were used as the gridded background field for typhoon wind vector prediction. For each matched typhoon sample, storm-centered ERA5 wind patches were extracted with a spatial size of 31 × 31 grids, corresponding to a physical area of approximately 7.75° × 7.75° (or ~860 km × ~860 km at the equator) at 0.25° resolution.

FY-3E WindRAD observations were obtained from the National Satellite Meteorological Center (NSMC) of the China Meteorological Administration. FY-3E was launched on 5 July 2021, and WindRAD, the first active microwave scatterometer for ocean surface wind measurement carried on the FY-3 series, provides ocean surface wind observations from C-band and Ku-band measurements; its performance was verified through an extended prelaunch and on-orbit commissioning and calibration campaign [24]. In this study, C-band, Ku-band, and Dual-band FY-3E WindRAD observations were considered. The study region covers East Asia, defined as 110°E–145°E and 5°N–40°N. The analysis is restricted to matched samples from 2023: for the 2023 typhoon season (May–November), a complete and consistent record covering all three bands is available, which supports the three-band comparison conducted in this study. Extending the evaluation to additional seasons will become possible as the operational data record matures, or through the incorporation of other scatterometer datasets; both directions are identified in the Conclusions.

Table 1 summarizes the data sources used in this study, including the CMA Best Track dataset for typhoon center positioning, ERA5 reanalysis for gridded wind fields, and FY-3E WindRAD Level-2 products from C-band, Ku-band, and Dual-band observations. The spatial and temporal resolutions of each dataset, along with their respective providers, are listed for reference.

Figure 1 shows the study region and typhoon tracks analyzed in this work. Panel (a) displays the geographic extent (110°E–145°E, 5°N–40°N) covering the western North Pacific and East Asian coastal waters. Panel (b) presents all CMA best-track points for 2023 typhoons, colored by intensity category according to the CMA classification. The majority of track points lie between 20°N and 30°N, consistent with the typical typhoon activity zone in this region.

Table 1. Summary of data sources and study area configuration.

Data Source	Variables	Spatial Resolution	Temporal Resolution	Provider
CMA Best Track	Typhoon center, max wind, min pressure	—	6 h	CMA
ERA5 reanalysis	10-m *u* wind, 10-m *v* wind	0.25° × 0.25°	1 h	ECMWF
FY-3E WindRAD (C-band)	Wind speed, wind direction, quality flag	25 km × 25 km	Orbit-dependent	NSMC/CMA
FY-3E WindRAD (Ku-band)	Wind speed, wind direction, quality flag	12.5 km × 12.5 km	Orbit-dependent	NSMC/CMA
FY-3E WindRAD (Dual-band)	Merged wind speed, wind direction	25 km × 25 km	Orbit-dependent	NSMC/CMA

Note: The study region is 110°E–145°E, 5°N–40°N. All experiments use 2023 typhoon samples. '—' indicates not applicable: the CMA Best Track dataset provides point records of storm center positions rather than gridded fields, so it has no fixed spatial resolution.

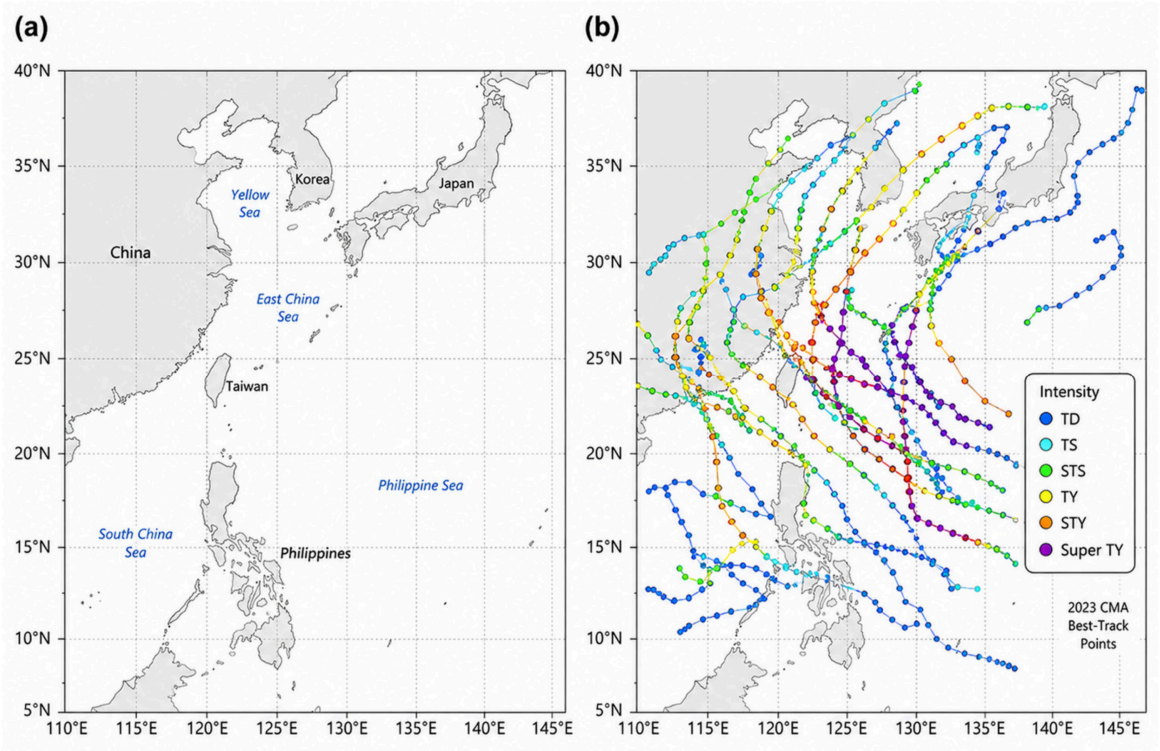


Figure 1. Study region and spatial distribution of 2023 typhoon best-track points used in this study. (**a**) Geographic extent of the study area covering the northwestern Pacific Ocean and East Asian coastal regions; (**b**) CMA best-track points for all typhoons in 2023, with color indicating typhoon intensity categories.

2.2. FY-3E Wind Vector Conversion

The original FY-3E WindRAD products provide wind speed, wind direction, latitude, longitude, quality flag, and time information. Table 2 summarizes the main FY-3E WindRAD Level-2 variables used in this study, including wind speed, wind direction, latitude, longitude, quality flag, and temporal information.

Table 2. FY-3E WindRAD Level-2 product variables used in this study.

Variable Name	Description	Scale Factor	Fill Value	Usage
wind_speed_selected	Retrieved stress-equivalent wind speed	0.01 m/s	32,767	Wind speed extraction
wind_dir_selected	Retrieved stress-equivalent wind direction	0.1°	32,767	Wind direction extraction
wvc_lat	Wind vector cell latitude	10^{-6}°	32,767	Spatial location
wvc_lon	Wind vector cell longitude	10^{-6}°	32,767	Spatial location
wvc_quality_flag	Quality control flag	—	32,767	Data filtering
day_count	Days since reference epoch	day	32,767	Temporal matching
millisecond_count	Milliseconds within the day	ms	32,767	Temporal matching

Note: All variables are scaled according to the product specification before preprocessing. '—' indicates not applicable: the quality flag is a dimensionless integer code and has no scale factor.

According to the metadata of the FY-3E WindRAD Level-2 Ocean Surface Wind Vector Product, the variables wind_speed_selected and wind_dir_selected represent the retrieved stress-equivalent wind speed and wind direction, respectively. The same definition is used for the C-band, Ku-band, and Dual-band products examined in this study. The original Level-2 metadata do not explicitly identify these variables as neutral or equivalent-neutral winds; therefore, they are referred to here according to the product definition as stress-equivalent winds. No additional stability, air-density, wind-height, or neutral-wind conversion was applied during preprocessing.

The raw wind speed and wind direction values were first scaled as follows:

$$\text{wind_speed} = \text{wind_speed_selected}/100 \tag{1}$$

$$\text{wind_direction} = \text{wind_dir_selected}/10 \tag{2}$$

Invalid values were removed according to the fill value definition. In particular, grid points with fill values such as 32,767 were excluded from the valid observation mask.

After quality control and application of the product-provided scaling factors, FY-3E wind speed and wind direction were converted into U and V wind vector components. The quality-control procedure followed the information provided in the WindRAD Level-2 product. According to the FY-3E WindRAD Level-2 product metadata, wind direction (dir) is provided in oceanographic convention, representing the direction toward which the wind blows, measured clockwise from true north (0° = north, 90° = east). Accordingly, the eastward (U) and northward (V) wind components were calculated as:

$$U = \text{ws}\ \sin(\text{dir}) \tag{3}$$

$$V = \text{ws}\ \cos(\text{dir}) \tag{4}$$

where ws denotes the retrieved stress-equivalent wind speed and dir denotes the oceanographic wind direction. A binary mask was further constructed to indicate whether each grid cell contained a valid FY-3E observation. Therefore, the FY-3E input contains three channels:

$$\text{FY-3E_input} = [\text{fy3e_u}, \text{fy3e_v}, \text{fy3e_mask}] \tag{5}$$

Figure 2 illustrates the complete FY-3E preprocessing workflow. Starting from raw Level-2 variables, the pipeline applies quality control, regional subsetting, and temporal matching with CMA typhoon centers. Storm-centered patches are then extracted with an observation mask, followed by coverage filtering to retain valid samples. The final supervised dataset combines ERA5 patches, FY-3E patches (u, v, mask), and target wind vector labels.

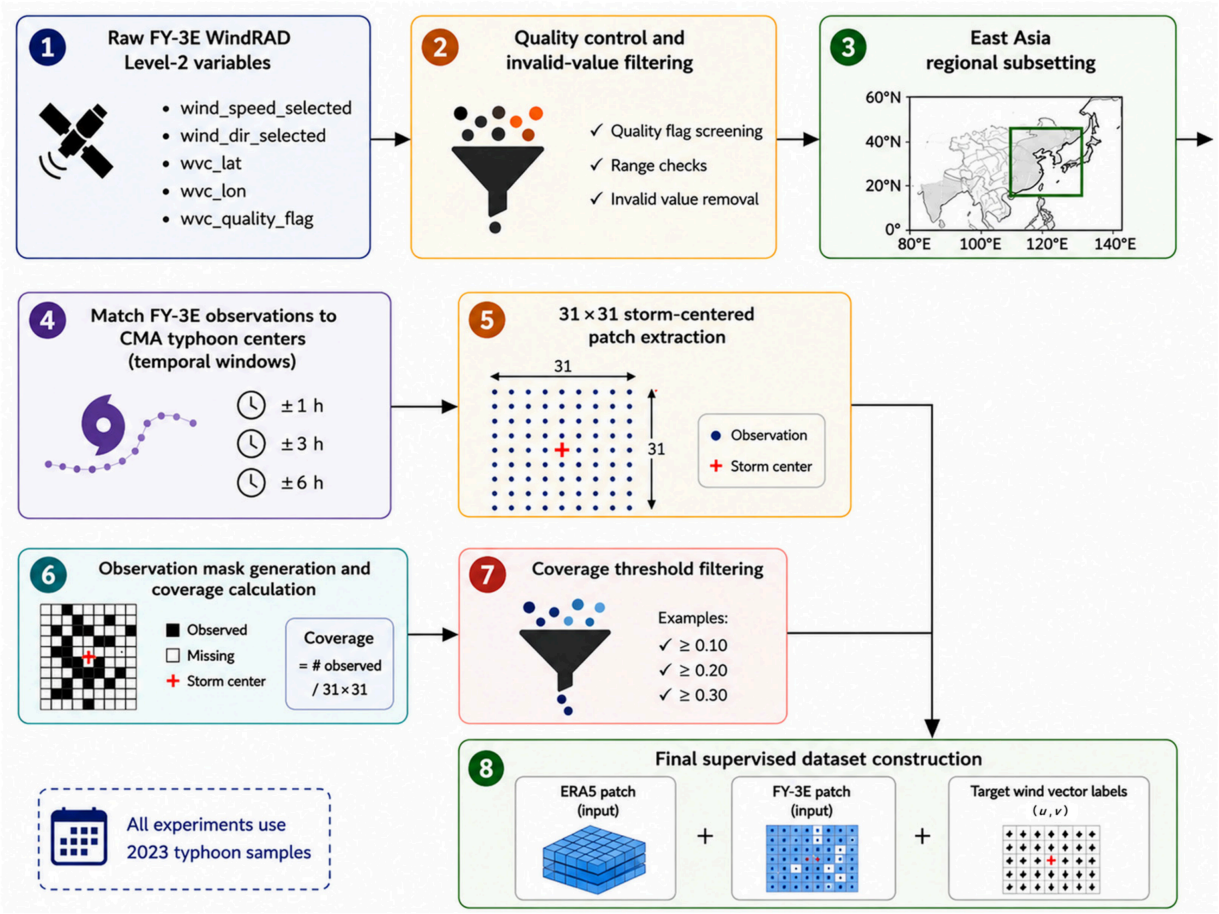


Figure 2. FY-3E WindRAD preprocessing and supervised dataset construction workflow. The circled numbers (1–8) indicate the order of the processing steps, and the boxes are color-coded by step for visual clarity. (**1**) Raw FY-3E WindRAD Level-2 variables; (**2**) Quality control and invalid-value filtering; (**3**) East Asia regional subsetting; (**4**) Temporal matching between FY-3E observations and CMA typhoon centers; (**5**) Storm-centered 31 × 31 patch extraction; (**6**) Observation mask generation and coverage calculation, where "# observed" denotes the number of valid observation grids and the coverage equals "# observed" divided by the total 31 × 31 grids (cf. Equation (6)); (**7**) Coverage threshold filtering; (**8**) Final supervised dataset construction with ERA5 patches, FY-3E patches, and target wind vector labels. The dashed box indicates that all experiments use 2023 typhoon samples.

2.3. Multimodal Sample Construction

Each supervised sample was constructed by aligning CMA typhoon records, ERA5 wind patches, and FY-3E WindRAD observations. The ERA5 input contains two channels, namely the ERA5 u and v wind components, with input shape $(N, 2, 31, 31)$.

In this study, the prediction task is formulated as a 12-h short-term typhoon wind vector prediction problem. For each sample, the atmospheric state at the reference time t_0 is used as input, while the future wind vector at $t_0 + 12$ h is defined as the prediction target. Specifically, the ground truth consists of the ERA5 10-m wind components at the future time step, including the zonal component $u_{ERA5}(t_0 + 12\,\mathrm{h})$ and meridional component $v_{ERA5}(t_0 + 12\,\mathrm{h})$. The two components are evaluated at the CMA best-track typhoon center position at $t_0 + 12$ h, obtained by bilinear interpolation of the ERA5 grid to the center longitude and latitude. The target is therefore a two-dimensional point value representing the future storm-center wind state, not a gridded wind field; the CMA best-track maximum wind speed is used only for describing storm intensity (e.g., in Figure 1), not as a regression target. Therefore, the model learns the mapping from the current multimodal observations to the future typhoon wind vector.

The FY-3E input contains the converted FY-3E u component, v component, and binary observation mask, with input shape (N, 3, 31, 31).

FY-3E observations were matched to each typhoon sample using temporal windows centered on the reference input time t_0. In the main experiments, candidate FY-3E observations within ± 3 h of t_0 were considered. When multiple FY-3E observations were available for the same sample, the candidate with the highest spatial coverage was preferentially selected, with the temporal difference used as an additional matching criterion. Because the ± 3 h window is symmetric around t_0, some matched FY-3E observations may occur after t_0. Therefore, this setting should be interpreted as a retrospective evaluation of the potential contribution of FY-3E observations rather than as a strictly real-time operational forecasting configuration. The prediction target remains fixed at $t_0 + 12$ h, and no ERA5 data after t_0 are used as model inputs. To evaluate the influence of temporal mismatch, additional experiments were conducted using ± 1 h and ± 6 h windows. After temporal matching, FY-3E observations within the storm-centered region were remapped to the $0.25^\circ \times 0.25^\circ$ ERA5 grid using nearest-neighbor interpolation. Each FY-3E wind vector cell (WVC) at native resolution (25 km for C-band, 12.5 km for Ku-band) was assigned to the nearest ERA5 grid cell center within the 31×31 storm-centered patch. When multiple FY-3E observations fell within the same ERA5 grid cell, the value closest in time to the reference time t_0 was retained. Coverage was then calculated as the proportion of valid FY-3E observation grids within the patch:

$$\text{coverage} = \frac{1}{H \times W} \times \sum_{i=1}^{H} \sum_{j=1}^{W} \text{mask}_{ij} \tag{6}$$

where $H = W = 31$ is the patch dimension, and $\text{mask}_{ij} \in \{0, 1\}$ indicates whether grid cell (i, j) contains a valid FY-3E observation (i.e., passing quality control and having non-fill values).

2.4. Coverage Filtering and Band Settings

Because FY-3E WindRAD observations are swath-dependent and spatially incomplete, different samples have different spatial coverage ratios. To evaluate the influence of observation availability, coverage filtering was applied to the matched FY-3E samples.

For the C-band coverage sensitivity experiment, three thresholds were tested:

- coverage ≥ 0.10
- coverage ≥ 0.20
- coverage ≥ 0.30

For the main band comparison experiments, coverage ≥ 0.20 was selected as the primary threshold. This choice represents a deliberate compromise: the $\geq$0.10 threshold retains more samples (N = 210) but introduces sparse observations that do not improve prediction (with ERA5-only performing best), while the $\geq$0.30 threshold provides denser coverage but reduces the sample size considerably (N = 160), increasing result variability and limiting model training stability. Therefore, the intermediate $\geq$0.20 threshold (N = 186) was chosen as the main configuration, with $\geq$0.10 and $\geq$0.30 serving as sensitivity bounds to evaluate the impact of coverage on fusion performance. Under this setting, C-band, Ku-band, and Dual-band observations were compared.

To ensure a fair comparison among different bands, an additional common-sample experiment was conducted. The common samples were obtained by taking the intersection of the sample indices shared by C-band, Ku-band, and Dual-band under coverage ≥ 0.20 and ± 3 h temporal matching. A total of 179 common samples were obtained, and the target labels were verified to be identical across the three band-specific datasets.

2.5. Dataset Partitioning and Repeated Experiments

For the main experiments, the matched samples were randomly divided at the sample level into training, validation, and test subsets with an approximate ratio of 7:1.5:1.5. The same split was used for all compared models under the same random seed to ensure a fair comparison. Because this random sample-level partition does not enforce separation by typhoon ID, samples from the same typhoon event may appear in different subsets. Therefore, the main experiments should be interpreted as evaluating prediction performance under random sample-level partitioning rather than strict generalization to completely unseen typhoon events. This ratio was chosen to preserve sufficient training samples for model convergence; preliminary experiments showed that reducing the training set below 65% of the total samples led to unstable validation loss and increased overfitting. The 7:1.5:1.5 split yields a test set of approximately 27–32 samples per random seed, which limits statistical power, but this trade-off is necessary given the limited sample size ($N \approx 184$–210) and the need for a stable training set.

To reduce the influence of random data partitioning, each experiment was repeated using five random seeds:

$$\text{seed} = 0, 1, 2, 3, 4$$

For reproducibility, all random seeds were fixed at the beginning of each experiment using torch.manual_seed(seed) and np.random.seed(seed) in PyTorch (version 2.0.1) and NumPy (version 1.24.3), respectively. The same set of five seeds was applied consistently across all experiments to control the randomness associated with data splitting and model initialization and to improve experimental reproducibility. In addition, torch.backends.cudnn.deterministic = True and torch.backends.cudnn.benchmark = False were used to reduce nondeterminism in CUDA-based computations. The final results are reported as the mean and standard deviation across the five repeated experiments.

To further assess storm-level generalization, we conducted a 5-fold group cross-validation (Group CV) using the official CMA storm number as the grouping variable. The 2023 matched datasets contain samples from 22 tropical cyclone systems (16 named storms and 6 unnamed tropical depressions; Supplementary Table S1). All samples belonging to the same storm were assigned exclusively to either the training or the test fold, and no storm appears on both sides of the training/test split in any fold (fold composition in Supplementary Table S2). Within each training fold, the training samples were further divided into training and validation subsets for early stopping. ERA5-only, naive fusion, mask-aware fusion, and gated fusion were evaluated under the same Group CV protocol. The results are presented in Section 3.6.

2.6. Overview of Experimental Models

This study evaluates whether FY-3E WindRAD observations can provide complementary information to ERA5 reanalysis for typhoon wind vector prediction. Rather than introducing a complex new operational forecasting system, we focus on a controlled comparison of several lightweight fusion strategies. Four model settings are considered: ERA5-only, naive ERA5–FY-3E fusion, mask-aware fusion, and gated fusion.

CNN-based encoders are adopted because the inputs are storm-centered gridded wind fields, for which the primary task is to extract spatial patterns of typhoon wind structures; lightweight convolutional architectures therefore provide an appropriate balance between spatial feature-extraction capability and model complexity under the limited-sample setting of this study.

The ERA5-only model uses only ERA5 u and v wind components as input. The fusion models use both ERA5 and FY-3E inputs. The FY-3E input consists of three channels: FY-3E u component, FY-3E v component, and a binary observation mask. All FY-3E wind vectors are generated using the method described in Section 2.

The ERA5 input and target formats are defined as follows:

$$\text{ERA5_input} = [\text{era5_u}, \text{era5_v}] \tag{7}$$

$$\text{Target} = [\text{label_u}, \text{label_v}] \tag{8}$$

The target is a two-dimensional future wind vector label consisting of ERA5-derived u and v components at $t_0 + 12$ h, which serves as the ground truth for evaluation. The purpose of the model comparison is to evaluate how different forms of FY-3E fusion affect wind vector prediction accuracy under different coverage thresholds, frequency bands, and temporal matching windows.

2.7. ERA5-Only Baseline

The ERA5-only baseline uses the ERA5 wind patch as the only input. The input tensor has two channels corresponding to the ERA5 u and v components:

$$x_{\text{ERA5}} \in \mathrm{R}^{(N\times 2\times 31\times 31)} \tag{9}$$

A lightweight convolutional neural network is used to encode the ERA5 wind patch. The network consists of three convolutional blocks. Table 3 details the architecture of each block.

Table 3. Architecture of the ERA5-only baseline CNN.

Layer	Configuration	Output Shape
Input	—	(N, 2, 31, 31)
Block 1	Conv2d(2, 32, k = 3, p = 1) → BN → ReLU → MaxPool(2 × 2)	(N, 32, 15, 15)
Block 2	Conv2d(32, 64, k = 3, p = 1) → BN → ReLU → MaxPool(2 × 2)	(N, 64, 7, 7)
Block 3	Conv2d(64, 128, k = 3, p = 1) → BN → ReLU	(N, 128, 7, 7)
Adaptive Pool	AdaptiveAvgPool(1 × 1)	(N, 128, 1, 1)
Flatten	—	(N, 128)
FC	Linear(128, 64) → ReLU → Linear(64, 2)	(N, 2)

Note: k = kernel size, p = padding, BN = Batch Normalization, FC = Fully Connected. AdaptiveAvgPool denotes adaptive average pooling. '—' indicates not applicable.

The extracted feature vector (128-dim) is then passed to a fully connected regression head to predict the two target wind components. This baseline provides the reference performance without FY-3E WindRAD observations. All fusion models are compared with this ERA5-only model under the same data split and random seed.

2.8. Naive Fusion and Mask-Aware Fusion

The naive fusion model directly concatenates ERA5 and FY-3E channels at the input level. Its input contains five channels:

$$x_{\text{naive}} = [\text{era5_u}, \text{era5_v}, \text{fy3e_u}, \text{fy3e_v}, \text{fy3e_mask}] \tag{10}$$

The input tensor shape is:

$$x_{\text{naive}} \in \mathrm{R}^{(N\times 5\times 31\times 31)} \tag{11}$$

This model tests whether simply adding FY-3E WindRAD observations as additional channels improves prediction performance. Since FY-3E observations are spatially sparse, direct concatenation may introduce discontinuous information when the satellite coverage is incomplete.

The mask-aware fusion model further includes masked FY-3E wind components:

$$\text{fy3e_u_masked} = \text{fy3e_u} \times \text{fy3e_mask} \tag{12}$$

$$\text{fy3e_v_masked} = \text{fy3e_v} \times \text{fy3e_mask} \tag{13}$$

Thus, the mask-aware input contains seven channels:

$$x_{\text{mask-aware}} = [\text{era5_u}, \text{era5_v}, \text{fy3e_u}, \text{fy3e_v}, \text{fy3e_mask}, \text{fy3e_u_masked}, \text{fy3e_v_masked}] \tag{14}$$

The purpose of this design is to explicitly provide the model with both the raw FY-3E wind components and the valid observed components constrained by the mask. The naive fusion and mask-aware fusion models use the same CNN backbone as the ERA5-only baseline, with only the number of input channels changed.

2.9. Gated Fusion Model

To better control the contribution of sparse FY-3E observations, a lightweight gated fusion model is introduced. Unlike naive fusion, the gated fusion model uses separate encoders for ERA5 and FY-3E inputs.

The ERA5 encoder takes two input channels, era5_u and era5_v.

The FY-3E encoder takes three input channels, fy3e_u, fy3e_v, and fy3e_mask.

Both encoders use convolutional layers to extract compact feature vectors. The FY-3E coverage ratio is also computed from the mask as:

$$\text{coverage} = \text{mean}(\text{fy3e_mask}) \tag{15}$$

The ERA5 feature, FY-3E feature, and coverage value are concatenated and passed through a small gate network. The gate is generated using fully connected layers and a sigmoid activation. The coverage ratio is introduced as an explicit auxiliary variable because FY-3E observations are spatially incomplete and their representativeness depends on observation availability. By incorporating coverage information into the gating mechanism, the model can adapt the contribution of FY-3E features under different observation coverage conditions during feature fusion.

$$\text{gate} = \text{sigmoid}(\text{MLP}([F_{\text{ERA5}}, F_{\text{FY3E}}, \text{coverage}])) \tag{16}$$

Specifically, the gate network takes the concatenation of the ERA5 feature vector (128-dim), the FY-3E feature vector (128-dim), and the scalar coverage ratio (1-dim), resulting in a 257-dimensional input. The gate network consists of Linear(257, 128) $\rightarrow$ ReLU $\rightarrow$ Linear(128, 128) $\rightarrow$ Sigmoid, producing a 128-dimensional feature-wise gate. The gated FY-3E representation is obtained by element-wise multiplication between the gate vector and the FY-3E feature vector.

$$F_{\text{FY3E_gated}} = \text{gate} \times F_{\text{FY3E}} \tag{17}$$

Finally, the ERA5 feature, gated FY-3E feature, and coverage value are concatenated and passed to a regression head to predict the target wind vector:

$$\text{output} = \text{Head}([F_{\text{ERA5}}, F_{\text{FY3E_gated}}, \text{coverage}]) \tag{18}$$

This design allows the model to adaptively adjust the contribution of FY-3E features according to the learned feature representation and the available observation coverage. When FY-3E information is useful, the model can increase the contribution of the FY-3E branch. When FY-3E observations are sparse or noisy, the model can rely more on ERA5 features.

Figure 3 illustrates the overall architecture. The ERA5 encoder branch extracts background wind-field features from the two-channel ERA5 input (u and v components), while the FY-3E encoder branch extracts satellite observation features from the three-channel FY-3E input (u, v, and mask). The coverage ratio, computed from the FY-3E mask, is concatenated with the feature vectors from both branches and passed through a gate network to generate an adaptive 128-dimensional feature-wise gate. This gate modulates the FY-3E feature representation through element-wise multiplication before final fusion with the ERA5 feature and coverage information.

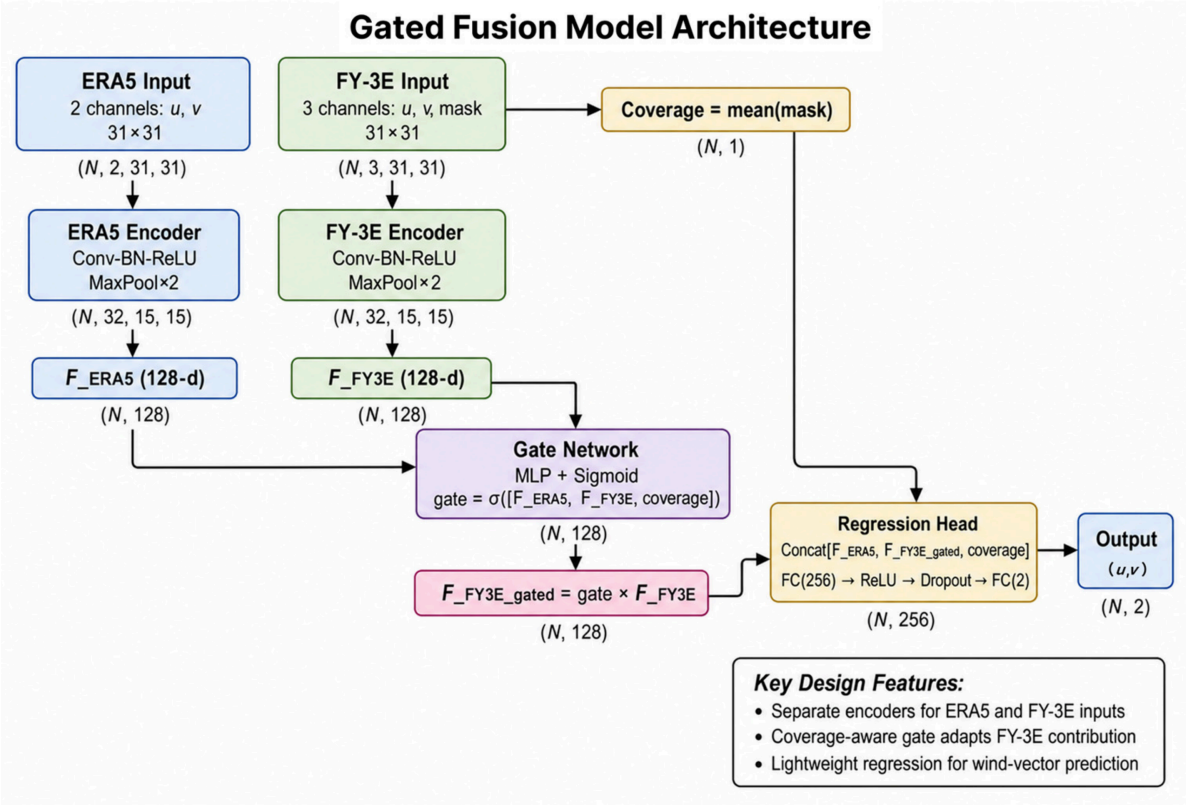


Figure 3. Architecture of the gated fusion model. Separate CNN encoders produce 128-dimensional ERA5 and FY-3E feature vectors. These features, together with the scalar coverage ratio, are used to generate a 128-dimensional feature-wise gate that adaptively modulates the FY-3E representation before final regression. Blue boxes denote the ERA5 encoder branch, green boxes denote the FY-3E encoder branch, orange boxes denote the coverage calculation and the regression head, and purple and pink boxes denote the gating pathway (the gate network and the gated FY-3E feature, respectively); arrows indicate the direction of data flow.

Figure 4 presents the complete multimodal sample construction workflow. Starting from raw FY-3E Level-2 variables, the pipeline applies quality control, regional subsetting, and temporal matching with CMA typhoon centers. Storm-centered 31 × 31 patches are then extracted from both ERA5 and FY-3E data, with an observation mask generated to indicate valid satellite grids. Coverage filtering retains samples meeting the threshold, and the final supervised dataset combines ERA5 patches, FY-3E patches (u, v, mask), and future wind vector labels for model training and evaluation.

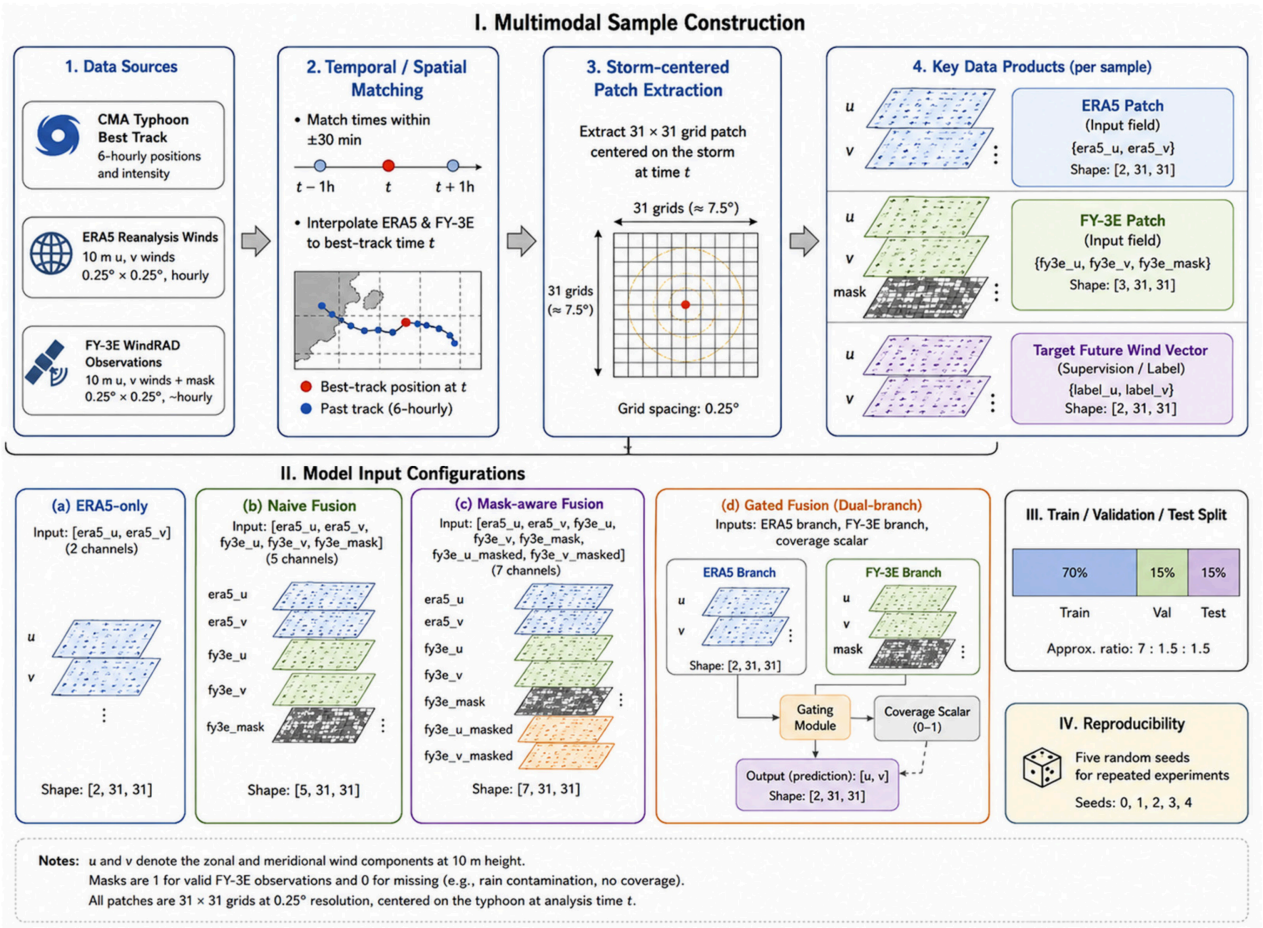


Figure 4. Multimodal sample construction and model input configuration. Colors denote the data sources and model components: blue indicates ERA5-related data and the ERA5 branch, green indicates FY-3E-related data and the FY-3E branch, purple indicates the target wind-vector labels and the model output, orange indicates the gating module, and gray indicates the coverage scalar. The thick gray arrows between steps 1–4 indicate the order of the sample-construction workflow; the thin arrows in panel (**d**) indicate the data flow of the gated fusion model, and the dashed arrows denote the coverage scalar feeding into the gating module. In steps 2 and 3, the red dot marks the best-track typhoon center at time t, and the blue dots mark the past 6-hourly track positions.

2.10. Training Configuration

All experiments are implemented using PyTorch. The models are trained with the Adam optimizer, an initial learning rate of 1×10^{-3}, and weight decay of 1×10^{-4}. The loss function is Smooth L1 loss. The batch size is set to 32, and the maximum number of training epochs is 300. Early stopping is applied with a patience of 40 epochs based on the validation loss.

The dataset partitioning and random seed protocol follow the same configuration as described in Section 2.5. All models in the same experiment use the same train/validation/test split under the same random seed to ensure a fair comparison.

Before training, input variables are normalized using the mean and standard deviation computed from the training subset only. The same normalization parameters are then applied to the validation and test subsets. This avoids information leakage from validation or test samples into the training process.

2.11. Comparison with Advanced Deep Learning Baselines

To ensure a rigorous evaluation of the proposed fusion strategies, we include three representative deep learning architectures as reference baselines. These models are selected to cover spatial-only, lightweight spatial, and attention-based paradigms that have been widely applied in meteorological prediction tasks [7,8,25,26]. All baselines are evaluated under the same data splits, random seeds, and evaluation metrics as the main experiments.

2.11.1. CNN-SE-MBFN with Channel Attention and Multi-Branch Fusion

The CNN-LSTM-SE-MBFN model proposed by [25] was originally designed for short-term typhoon wind field prediction using four consecutive hourly frames of ERA5 reanalysis data, combining CNN-based spatial feature extraction, LSTM-based temporal modeling, squeeze-and-excitation (SE) channel attention, and a multi-branch feature fusion network (MBFN) with 1×1, 3×3, and 5×5 convolutional branches.

Because the current FY-3E–ERA5 fusion task uses single-frame inputs rather than temporal sequences, we adapt this architecture for our regression setting. The specific modifications are as follows: (1) the LSTM temporal module is completely removed, as only a single time step is used; (2) the CNN spatial encoder, SE channel attention module, and MBFN multi-scale convolutional branches are retained to preserve multi-scale spatial feature extraction capability; (3) global average pooling is applied after the MBFN output to collapse the spatial dimensions; and (4) the original gridded wind field prediction head is replaced with a two-dimensional wind vector regression head consisting of Linear(128, 64) $\rightarrow$ ReLU $\rightarrow$ Linear(64, 2). The SE module uses a reduction ratio of 8, and the MBFN branches use 16 filters each. This adapted architecture has approximately 177,000 parameters.

2.11.2. U-Net Encoder

U-Net is a classic encoder–decoder architecture widely used in meteorological image-to-image prediction tasks [7]. For the current vector regression task, we retain the encoder path (two downsampling blocks with double convolutions) and replace the decoder with a global average pooling layer followed by a fully connected regression head. This lightweight variant preserves U-Net's strong spatial feature extraction capability while adapting the output format to two-dimensional wind vector prediction. The architecture has approximately 321,000 parameters.

2.11.3. Vision Transformer (ViT)

Transformer-based models have recently shown promise in weather forecasting due to their global attention mechanism [9,26]. More recently, GraphCast demonstrated skillful medium-range global weather forecasting using graph neural networks [27], though its application to typhoon-specific short-term prediction remains limited. We implement a lightweight patch-based Transformer with a patch size of 4×4, yielding 49 patches from the 31×31 input. The patch size of 4×4 was selected to balance spatial resolution and computational efficiency. This yields 49 patches (7×7), which is sufficient for the self-attention mechanism to capture spatial relationships across the storm-centered wind field while maintaining a manageable sequence length. Larger patches (e.g., 8×8) would reduce spatial resolution and potentially lose fine-scale wind structure, whereas smaller patches (e.g., 2×2) would increase sequence length and computational cost without clear benefit given the limited sample size. The model uses 4 Transformer encoder layers with 4 attention heads and an embedding dimension of 128. This baseline evaluates whether global self-attention can outperform local convolutional inductive biases for sparse satellite–reanalysis fusion. The architecture has approximately 557,000 parameters.

2.11.4. Input Configuration for Fair Comparison

All baseline models are evaluated under two input configurations to isolate the effect of FY-3E fusion.

The two configurations serve distinct purposes: ERA5-only establishes the baseline performance of each architecture without satellite data, while ERA5 + FY-3E tests whether the same architecture can effectively exploit sparse scatterometer observations. Comparing these configurations across models reveals whether the fusion benefit is architecture-dependent or generalizes across different inductive biases.

ERA5-only: Input channels = 2 (ERA5 u and v components). This tests whether the baseline architectures themselves improve over the simple CNN used in Section 2.7.

ERA5 + FY-3E naive fusion: Input channels = 5 (ERA5 u and v, FY-3E u and v, and the FY-3E mask). This tests whether adding FY-3E data to a representative baseline yields better results than adding it to a simple CNN.

All models use the same training configuration described in Section 2.10 (Adam optimizer, learning rate 1×10^{-3}, Smooth L1 loss, batch size 32, 300 epochs, early stopping with patience 40) and the same five random seeds (0–4). The same train/validation/test splits are used for all models under each seed.

2.12. Comparison Settings

The comparison settings are designed to evaluate the effect of FY-3E WindRAD fusion from multiple perspectives.

First, coverage sensitivity experiments are conducted using C-band observations under three coverage thresholds: coverage ≥ 0.10, coverage ≥ 0.20, and coverage ≥ 0.30. This experiment examines how the availability of FY-3E observations affects model performance.

Second, band comparison experiments are conducted under coverage ≥ 0.20 and ± 3 h temporal matching. C-band, Ku-band, and Dual-band observations are compared to evaluate the influence of different FY-3E WindRAD bands.

Third, a common-sample fair comparison is performed by taking the intersection of the sample indices shared by C-band, Ku-band, and Dual-band. This ensures that the band comparison is not affected by differences in matched sample composition.

Fourth, time-window sensitivity experiments are conducted using Ku-band observations. The temporal matching windows include ± 1 h, ± 3 h, and ± 6 h. This experiment evaluates the trade-off between sample availability and temporal mismatch.

Fifth, benchmark comparison experiments are conducted using advanced deep learning architectures as representative baselines, including an adapted CNN-SE-MBFN model [25], U-Net Encoder, and Vision Transformer. These baselines are retrained under the same FY-3E + ERA5 fusion dataset to ensure a controlled evaluation.

2.13. Evaluation Metrics

The model predicts a two-dimensional wind vector consisting of u and v components. The evaluation metrics include Vector_MAE, Vector_RMSE, and average wind speed error (AWSE).

Vector_MAE measures the mean Euclidean distance between predicted and target wind vectors:

$$\text{Vector_MAE} = \text{mean}(\sqrt{\left(u_{\text{pred}} - u_{\text{true}}\right)^2 + \left(v_{\text{pred}} - v_{\text{true}}\right)^2}) \quad (19)$$

Vector_RMSE measures the root mean square wind vector error:

$$\text{Vector_RMSE} = \sqrt{\text{mean}(\left(u_{\text{pred}} - u_{\text{true}}\right)^2 + \left(v_{\text{pred}} - v_{\text{true}}\right)^2)} \quad (20)$$

AWSE measures the absolute error of wind speed magnitude:

$$\mathrm{AWSE} = \mathrm{mean}(\left|\sqrt{{u_{\mathrm{pred}}}^2 + {v_{\mathrm{pred}}}^2} - \sqrt{{u_{\mathrm{true}}}^2 + {v_{\mathrm{true}}}^2}\right|) \quad (21)$$

Vector_MAE and Vector_RMSE evaluate the overall wind vector prediction error, while AWSE focuses on the error in wind speed magnitude. Lower values indicate better prediction performance. During manuscript preparation, large language models (ChatGPT-4, OpenAI, version GPT-4, July 2026; Kimi, Moonshot AI, version k2.6, July 2026) were used solely for English language polishing and formatting; the full statement is provided in the Acknowledgments.

3. Results

3.1. Coverage Sensitivity and Fusion Strategy Comparison

To evaluate the influence of FY-3E WindRAD observation coverage on ERA5-based typhoon wind vector prediction, we first conducted a coverage sensitivity experiment using the C-band observations. All FY-3E wind speed and wind direction observations were converted into wind vector components following the method described in Section 2. The temporal matching window was fixed at ±3 h, and three coverage thresholds were tested: coverage ≥ 0.10, coverage ≥ 0.20, and coverage ≥ 0.30.

For each coverage threshold, four model settings were compared: ERA5-only, ERA5 + FY-3E naive fusion, ERA5 + FY-3E mask-aware fusion, and ERA5 + FY-3E gated fusion. Each experiment was repeated with five random seeds, and the mean and standard deviation of the evaluation metrics are reported. The dataset was randomly divided into training, validation, and test subsets with an approximate ratio of 7:1.5:1.5 under each seed.

Table 4 summarizes the coverage sensitivity results for C-band observations. Statistical significance of the differences between each fusion model and the ERA5-only baseline was assessed using paired *t*-tests across the five random seeds.

Table 4. Coverage sensitivity and fusion strategy comparison for C-band FY-3E WindRAD observations.

Coverage Threshold	Sample Count	Model	Vector_MAE	Vector_RMSE	AWSE	BH-Adjusted *p*-Value [a]
≥0.10	210	ERA5-only	5.095 ± 0.370	5.789 ± 0.373	3.260 ± 0.458	—
≥0.10	210	Naive fusion	5.133 ± 0.409	5.876 ± 0.399	3.339 ± 0.303	0.9086
≥0.10	210	Mask-aware fusion	5.363 ± 0.395	6.026 ± 0.454	3.680 ± 0.374	0.7632
≥0.10	210	Gated fusion	5.182 ± 0.241	5.879 ± 0.262	3.354 ± 0.333	0.9086
≥0.20	186	ERA5-only	5.357 ± 0.671	6.045 ± 0.787	3.398 ± 0.693	—
≥0.20	186	Naive fusion	5.071 ± 0.629	5.812 ± 0.800	3.336 ± 0.438	0.9291
≥0.20	186	Mask-aware fusion	5.848 ± 0.464	6.570 ± 0.588	4.029 ± 0.632	0.7632
≥0.20	186	Gated fusion	5.323 ± 0.244	5.961 ± 0.220	3.520 ± 0.544	0.9605
≥0.30	160	ERA5-only	5.437 ± 0.957	6.092 ± 0.857	3.783 ± 1.093	—
≥0.30	160	Naive fusion	5.446 ± 0.632	5.954 ± 0.693	3.813 ± 0.156	0.9605
≥0.30	160	Mask-aware fusion	5.532 ± 0.762	6.071 ± 0.810	3.843 ± 0.535	0.9989
≥0.30	160	Gated fusion	5.427 ± 0.778	6.042 ± 0.867	3.783 ± 0.584	0.9717

Note: [a] Statistical comparisons are based on paired *t*-tests of Vector_RMSE between each fusion model and the corresponding ERA5-only baseline across the same five random seeds. Reported values are Benjamini–Hochberg-adjusted *p*-values obtained from the study-wide set of 37 unique prespecified comparisons across the study, controlling the false discovery rate at $q = 0.05$. '—' indicates not applicable.

To account for the multiple comparisons conducted across coverage thresholds, frequency bands, fusion models, and evaluation metrics, we applied the Benjamini–Hochberg false discovery rate (FDR) procedure [28] to control the expected proportion of false posi-

tives. All p-values reported in this section and subsequent sections were adjusted within a single study-wide family of 37 prespecified comparisons at an FDR level of $q = 0.05$. After Benjamini–Hochberg FDR correction, none of the tested fusion improvements remained statistically significant at the $q = 0.05$ level. Therefore, the observed performance differences are interpreted primarily as numerical trends, and their robustness is further examined through effect-size analysis, common-sample comparison, and Group CV.

The results show that the effect of FY-3E WindRAD fusion is sensitive to the spatial coverage threshold. When the coverage threshold is relatively low (coverage ≥ 0.10), ERA5-only achieves the lowest Vector_RMSE and AWSE. This suggests that low-coverage FY-3E observations may introduce sparse and discontinuous information, which does not necessarily improve the prediction performance when directly fused with ERA5 fields.

When the coverage threshold increases to coverage ≥ 0.20, the naive fusion model obtains the lowest Vector_MAE, Vector_RMSE, and AWSE among the four settings. Compared with ERA5-only, the Vector_RMSE decreases from 6.045 to 5.812 (approximately 3.9% relative improvement). Given the limited sample size ($N = 186$ after coverage filtering), we cannot draw a definitive conclusion that C-band fusion consistently improves prediction performance. The observed improvement may reflect a genuine but modest signal that could become significant with a larger dataset, or it may be attributable to random variation in the particular data partitions used across the five random seeds. The effect size, measured by Cohen's d [29], was 0.28 for this comparison, indicating a small effect that is consistent with the lack of statistical significance. Therefore, while C-band observations show potential for providing complementary information under moderate coverage, the current evidence is insufficient to confirm their benefit conclusively. The mask-aware model performs worse than ERA5-only under this setting, while the gated fusion model shows a moderate reduction in Vector_RMSE but does not achieve the best result.

For coverage ≥ 0.30, the number of available samples decreases from 210 to 160. Although naive fusion still achieves the lowest Vector_RMSE, the overall differences among models become small and the standard deviations increase.

Overall, the C-band coverage sensitivity experiment indicates that FY-3E WindRAD fusion is not automatically beneficial. Its contribution depends on the balance between observation coverage, sample size, and fusion strategy. In the current C-band setting, coverage ≥ 0.20 provides a relatively balanced configuration, while too low coverage may introduce sparse observation noise and too high coverage may reduce the effective sample size. Therefore, coverage ≥ 0.20 is used as the main threshold for the subsequent band comparison and common-sample experiments.

3.2. C/Ku/Dual Band Comparison

After determining coverage ≥ 0.20 as the main coverage threshold, we further compared the effects of different FY-3E WindRAD bands on typhoon wind vector prediction. Three band settings were evaluated: C-band, Ku-band, and Dual-band. For all bands, the temporal matching window was fixed at ± 3 h. Each experiment was repeated using five random seeds.

It should be noted that this section compares the performance of different bands on their own matched sample sets. Due to differences in orbital coverage and quality-controlled observations, the available sample numbers are slightly different among the three bands. Therefore, this section provides a band-specific comparison, while a stricter common-sample fair comparison is presented in Section 3.3.

Table 5 summarizes the performance of ERA5-only, naive fusion, mask-aware fusion, and gated fusion for the three FY-3E WindRAD band settings, with statistical significance annotations.

Table 5. Band-specific comparison under coverage ≥ 0.20 and ± 3 h temporal matching.

Band	Model	Vector_MAE	Vector_RMSE	AWSE	BH-Adjusted *p*-Value [a]
C-band	ERA5-only	5.357 ± 0.671	6.045 ± 0.787	3.398 ± 0.693	—
C-band	Naive fusion	5.071 ± 0.629	5.812 ± 0.800	3.336 ± 0.438	0.9291
C-band	Mask-aware fusion	5.848 ± 0.464	6.570 ± 0.588	4.029 ± 0.632	0.7632
C-band	Gated fusion	5.323 ± 0.244	5.961 ± 0.220	3.520 ± 0.544	0.9605
Ku-band	ERA5-only	5.091 ± 0.432	5.736 ± 0.640	3.597 ± 0.672	—
Ku-band	Naive fusion	5.198 ± 0.712	5.877 ± 0.841	3.720 ± 0.764	0.9086
Ku-band	Mask-aware fusion	5.107 ± 0.381	5.735 ± 0.558	3.600 ± 0.503	0.9989
Ku-band	Gated fusion	4.690 ± 0.469	5.366 ± 0.642	3.276 ± 0.565	0.8256
Dual-band	ERA5-only	5.060 ± 0.753	5.793 ± 0.920	3.476 ± 0.571	—
Dual-band	Naive fusion	5.285 ± 0.882	5.952 ± 0.910	3.851 ± 0.849	0.9086
Dual-band	Mask-aware fusion	5.257 ± 0.709	5.952 ± 0.805	3.731 ± 0.636	0.9086
Dual-band	Gated fusion	5.240 ± 0.747	5.900 ± 0.812	3.695 ± 0.823	0.9086

Note: [a] Statistical comparisons are based on paired *t*-tests of Vector_RMSE between each fusion model and the corresponding ERA5-only baseline across the same five random seeds. Reported values are Benjamini–Hochberg-adjusted *p*-values obtained from the study-wide set of 37 unique prespecified comparisons across the study, controlling the false discovery rate at $q = 0.05$. '—' indicates not applicable.

Under the band-specific evaluation, Ku-band gated fusion showed the clearest numerical improvement relative to the ERA5-only baseline. The corrected results reduced Vector_RMSE from 5.736 to 5.366 m/s and AWSE from 3.597 to 3.276 m/s. However, these improvements did not remain statistically significant after multiple-comparison correction. In contrast, Dual-band gated fusion did not outperform the ERA5-only baseline, indicating that combining C- and Ku-band observations does not necessarily provide additional predictive benefit under the current sample setting. Overall, the band-specific results suggest that the contribution of FY-3E observations is frequency-band dependent and should be interpreted as a conditional numerical improvement rather than a consistently significant advantage.

For Dual-band, the corrected results do not show an advantage over the ERA5-only baseline. One possible explanation is that C- and Ku-band retrievals have different error characteristics, and the current fusion architecture may not fully exploit their complementary information. Future work could consider band-specific feature encoders and the separate use of C- and Ku-band quality-control information before fusion, which may help reduce the effect of heterogeneous retrieval errors [30,31].

To further visualize the band-dependent prediction behavior, Figure 5 presents the ERA5 wind-speed background together with the reference and predicted center wind vectors under different band settings; the blue and red arrows denote the ERA5-derived reference and predicted vectors, respectively, and the numerical values indicate the target wind-speed magnitude in (a) and the center wind-vector error in (b–h). Panels (c,d), (e,f), and (g,h) show naive and gated fusion for the C-, Ku-, and Dual-band cases, respectively; the representative cases are the same as those in Figure 6.

Figure 6 compares the wind-vector prediction errors for the same representative cases: each panel shows the ERA5-derived reference (blue), predicted (red), and error (black dashed) vectors at the storm center, with lengths proportional to their magnitudes, so that the error can be compared visually across methods; quantitative comparisons across all test samples are provided in Table 5. Panels (a–c) show the C-band setting, (d,e) the Ku-band setting, and (f,g) the Dual-band setting.

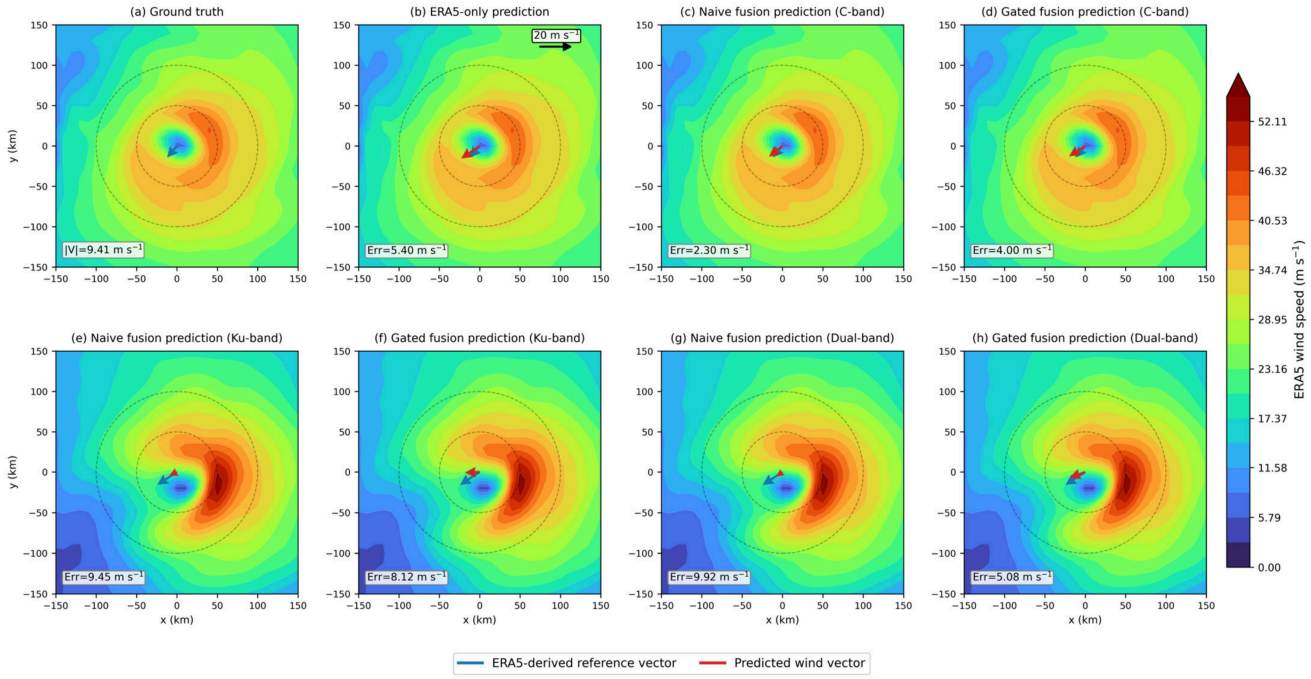


Figure 5. ERA5 wind-speed background and wind-vector comparison under different FY-3E band settings (coverage ≥ 0.20, ± 3 h temporal matching). (**a**) ERA5-derived reference target; (**b**) ERA5-only prediction; (**c**,**d**) naive and gated fusion with C-band observations; (**e**,**f**) with Ku-band observations; (**g**,**h**) with Dual-band observations. The blue arrow denotes the ERA5-derived reference vector and the red arrow the predicted center wind vector; dashed circles mark 50 and 100 km radii from the storm center. Numerical values indicate the target wind-speed magnitude in (**a**) and the center wind-vector error (m s^{-1}) in (**b**–**h**).

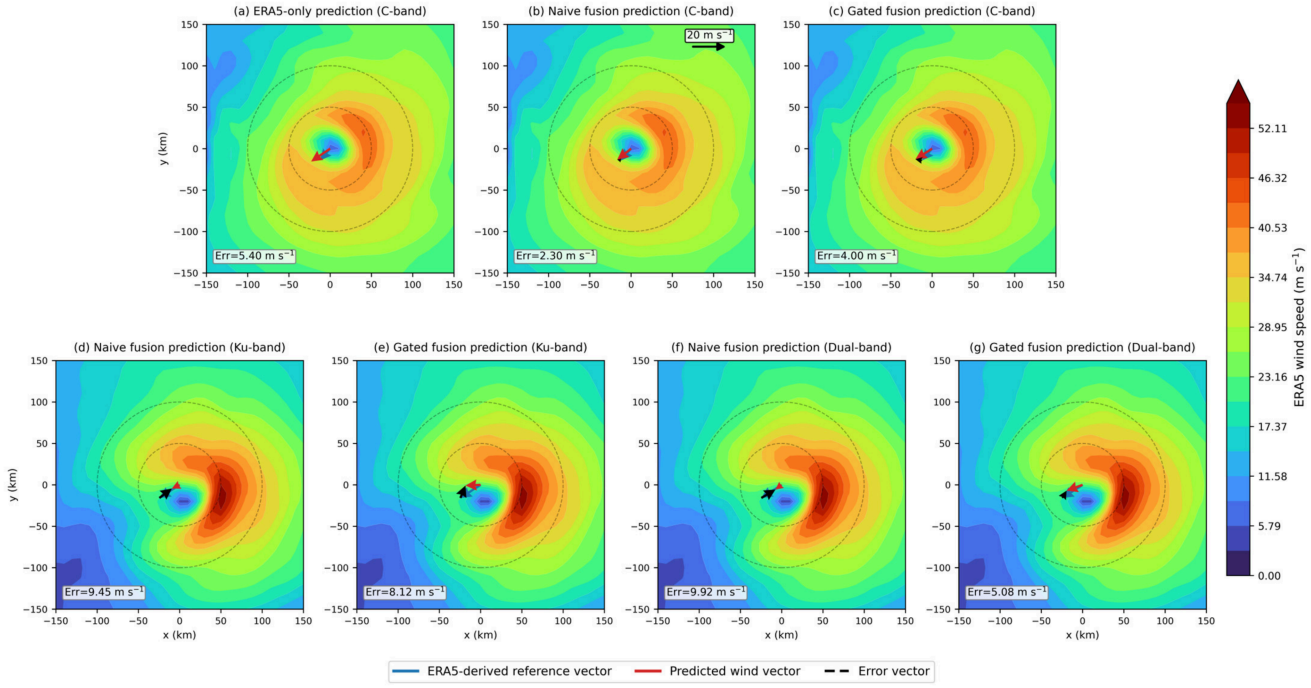


Figure 6. Center wind-vector error comparison under different FY-3E band settings (coverage ≥ 0.20, ± 3 h temporal matching). (**a**–**c**) ERA5-only, naive fusion, and gated fusion with C-band observations; (**d**,**e**) with Ku-band observations; (**f**,**g**) with Dual-band observations. The blue and red arrows denote the ERA5-derived reference and predicted center wind vectors, respectively, and the black dashed arrow denotes the error vector from the reference-vector tip to the predicted-vector tip; arrow lengths

are proportional to vector magnitudes (see the 20 m s^{-1} scale in panel (**b**)). Dashed circles mark 50 and 100 km radii from the storm center. Numerical values indicate the center wind-vector error (m s^{-1}).

Overall, the band comparison demonstrates band-dependent numerical behavior in FY-3E WindRAD fusion. In the band-specific experiments, Ku-band shows the most consistent numerical tendency, especially when combined with gated fusion. C-band shows partial improvement but is sensitive to the fusion strategy, while Dual-band does not show a clear advantage under its own matched samples. These results suggest that the effectiveness of FY-3E fusion is conditional rather than automatic, and band selection is an important factor in multimodal typhoon wind prediction.

3.3. Common-Sample Fair Comparison

Although the band-specific comparison in Section 3.2 provides an initial evaluation of different FY-3E WindRAD bands, the matched samples are not exactly identical among C-band, Ku-band, and Dual-band. The differences in sample composition may affect the comparison results. Therefore, to further ensure a fair evaluation, we constructed a common-sample subset by taking the intersection of the sample indices shared by all three bands under the same coverage ≥ 0.20 and ± 3 h temporal matching setting.

A total of 179 common samples were obtained. After alignment, the target labels of the three band-specific datasets were checked, and the maximum label difference between C-band and Ku-band, as well as between C-band and Dual-band, was 0.0. This confirms that the three FY-3E band inputs were evaluated on exactly the same typhoon samples with identical target labels.

Under this common-sample setting, four models were compared: ERA5-only, C-band + gated fusion, Ku-band + gated fusion, and Dual-band + gated fusion. Each experiment was repeated with five random seeds, using the same training, validation, and test split under each seed.

Table 6 reports the common-sample fair comparison results, with statistical significance annotations relative to the ERA5-only baseline.

Table 6. Common-sample fair comparison among C-band, Ku-band, and Dual-band under coverage ≥ 0.20 and ± 3 h temporal matching.

Model	Vector_MAE	Vector_RMSE	AWSE	BH-Adjusted *p*-Value [a]
ERA5-only	5.046 ± 0.808	5.721 ± 0.893	3.372 ± 0.627	—
C-band + Gated fusion	5.078 ± 0.685	5.658 ± 0.695	3.331 ± 0.572	0.9605
Ku-band + Gated fusion	5.148 ± 0.670	5.714 ± 0.704	3.344 ± 0.631	0.9989
Dual-band + Gated fusion	5.215 ± 0.668	5.791 ± 0.728	3.536 ± 0.482	0.9605

Note: [a] Statistical comparisons are based on paired *t*-tests of Vector_RMSE between each fusion model and the common-sample ERA5-only baseline across the same five random seeds. Reported values are Benjamini–Hochberg-adjusted *p*-values obtained from the study-wide set of 37 unique prespecified comparisons across the study, controlling the false discovery rate at $q = 0.05$. '—' indicates not applicable.

Before interpreting these results, it is important to acknowledge a key limitation: the common-sample experiment uses only 179 samples. With this small sample size, the test set in each random split contains only approximately 27 samples, which severely limits statistical power. To detect a 5% relative improvement in Vector_RMSE with 80% power and $\alpha = 0.05$, a post-hoc power analysis indicates that approximately 200 test samples would be needed. Our test set of approximately 27 samples provides only about 25% power, meaning that even moderate effect sizes are unlikely to reach statistical significance. The 95% confidence intervals for the observed differences are correspondingly wide. For example, the Ku-

band common-sample Vector_RMSE difference of only −0.007 m/s (5.714 vs. 5.721 m/s) is statistically indeterminate, and the Dual-band difference (+0.070 m/s, 5.791 vs. 5.721 m/s) likewise falls within the range of sampling variability. The effect sizes for these comparisons, measured by Cohen's *d*, are negligible, consistent with the lack of statistical significance. Therefore, the lack of statistical significance in this experiment should not be interpreted as evidence of no effect; rather, it reflects the inherent difficulty of detecting modest but potentially meaningful improvements with the current sample size. The results should be viewed as indicative trends that require validation with larger multi-year datasets.

Under the common-sample evaluation, the differences among the models became substantially smaller, and neither Ku-band nor Dual-band showed a clear advantage over the ERA5-only baseline (Table 6); this differs from the band-specific evaluation in Section 3.2, where Ku-band showed the clearest numerical improvement, because the band-specific datasets contain slightly different matched samples. Overall, the common-sample comparison indicates that the relative performance of different WindRAD bands is sensitive to sample composition; the results therefore do not support a universally superior frequency band under the current dataset and should be interpreted as conditional numerical differences rather than robust performance gains.

3.4. Time-Window Sensitivity Analysis

The temporal difference between a FY-3E WindRAD overpass and the corresponding typhoon sample may strongly influence the usefulness of satellite observations. A narrow temporal window can provide better consistency between FY-3E observations and the target typhoon state, but it may lead to a limited number of matched samples. In contrast, a wider temporal window increases the number of available samples but may introduce temporal mismatch noise, because typhoon wind fields can evolve rapidly within several hours.

To evaluate this effect, we conducted a time-window sensitivity experiment using Ku-band observations. Ku-band was selected because it showed the clearest improvement in the band-specific comparison. The coverage threshold was fixed at coverage ≥ 0.20, and three temporal matching windows were considered: ± 1 h, ± 3 h, and ± 6 h. All FY-3E wind vectors were generated using the same method.

Table 7 summarizes the sample availability under different temporal matching windows.

Table 7. Sample availability under different temporal matching windows for Ku-band observations.

Time Window	Matched Samples	Samples After Coverage $\geq$ 0.20	Training Setting
± 1 h	38	Not used for training	Too few samples for stable training
± 3 h	257	184	Main setting
± 6 h	486	366	Wider-window comparison

The ± 1 h setting provides the strictest temporal matching. However, only 38 samples were matched, which is insufficient for stable deep learning training and multi-seed evaluation. Therefore, this setting was used only to describe sample availability and was not included in the supervised training comparison.

The ± 3 h setting provides a practical balance between temporal consistency and sample availability. Under coverage ≥ 0.20, 184 samples remained for supervised training. As shown in Table 8, the corrected Ku-band results retain a numerical advantage for gated fusion relative to ERA5-only, although the improvement does not remain statistically significant after multiple-comparison correction. Therefore, the ± 3 h result should be interpreted as a numerical tendency rather than a statistically confirmed gain.

Table 8. Ku-band fusion performance under the ±3 h temporal matching window.

Model	Vector_MAE	Vector_RMSE	AWSE	BH-Adjusted *p*-Value [a]
ERA5-only	5.091 ± 0.432	5.736 ± 0.640	3.597 ± 0.672	—
Naive fusion	5.198 ± 0.712	5.877 ± 0.841	3.720 ± 0.764	0.9086
Mask-aware fusion	5.107 ± 0.381	5.735 ± 0.558	3.600 ± 0.503	0.9989
Gated fusion	4.690 ± 0.469	5.366 ± 0.642	3.276 ± 0.565	0.8256

Note: [a] Statistical comparisons are based on paired *t*-tests of Vector_RMSE between each fusion model and the ERA5-only baseline across the same five random seeds. Reported values are Benjamini–Hochberg-adjusted *p*-values obtained from the study-wide set of 37 unique prespecified comparisons across the study, controlling the false discovery rate at $q = 0.05$. This comparison is identical to the Ku-band comparison in Table 5 and is therefore included only once in the study-wide FDR correction. '—' indicates not applicable.

For the ±6 h setting, the number of available samples increased substantially. After coverage filtering, 366 samples were retained for supervised training. However, as shown in Table 9, the larger sample size did not lead to better fusion performance.

Table 9. Ku-band fusion performance under the ±6 h temporal matching window.

Model	Vector_MAE	Vector_RMSE	AWSE	BH-Adjusted *p*-Value [a]
ERA5-only	4.780 ± 0.207	5.430 ± 0.253	3.266 ± 0.145	—
Naive fusion	4.884 ± 0.204	5.499 ± 0.224	3.393 ± 0.304	0.9086
Mask-aware fusion	4.960 ± 0.276	5.622 ± 0.282	3.550 ± 0.258	0.8256
Gated fusion	5.022 ± 0.124	5.675 ± 0.115	3.454 ± 0.173	0.7632

Note: [a] Statistical comparisons are based on paired *t*-tests of Vector_RMSE between each fusion model and the ERA5-only baseline across the same five random seeds. Reported values are Benjamini–Hochberg-adjusted *p*-values obtained from the study-wide set of 37 unique prespecified comparisons across the study, controlling the false discovery rate at $q = 0.05$. '—' indicates not applicable.

Under the ±6 h setting, all three corrected FY-3E fusion configurations yielded higher Vector_RMSE than the ERA5-only baseline. Naive fusion, mask-aware fusion, and gated fusion produced Vector_RMSE values of 5.499, 5.622, and 5.675 m/s, respectively, compared with 5.430 m/s for ERA5-only. None of these differences remained statistically significant after study-wide Benjamini–Hochberg correction. Thus, increasing the number of matched samples under the wider temporal window did not translate into improved predictive performance.

The degradation observed under the ±6 h setting may be related to the reduced temporal representativeness of FY-3E observations: typhoon wind fields evolve rapidly through storm translation, intensity changes, and variations in internal structure, so observations acquired farther from the reference time carry a larger mismatch relative to the ERA5 target state, and their spatial distribution within the storm-centered patch also varies with overpass time. These factors reduce the benefit of incorporating FY-3E information when the temporal window becomes too wide.

Overall, the time-window sensitivity analysis suggests that temporal matching is an important factor affecting FY-3E WindRAD fusion performance. In the current dataset, the ±3 h temporal matching window provides a practical balance between sample availability and temporal consistency, and is therefore adopted as the main configuration for subsequent experiments.

3.5. Benchmark Comparison with Advanced Deep Learning Models

To evaluate whether the fusion strategy improves on baseline architecture selection, we compare the gated fusion model with three representative architectures (CNN-SE-MBFN [25], U-Net Encoder, and Vision Transformer) that are retrained under the identical

Ku-band setting (coverage ≥ 0.20, ± 3 h temporal matching), data splits, random seeds, and evaluation metrics; the architecture details are given in Section 2.11.

3.5.1. ERA5-Only Baseline Comparison

Table 10 reports the performance of all models using ERA5-only inputs. This experiment isolates the intrinsic predictive capability of each architecture without FY-3E satellite observations.

Table 10. ERA5-only baseline comparison under Ku-band matched samples.

Model	Vector_MAE	Vector_RMSE	AWSE	Parameters (M)
Gated Fusion ERA5-only	4.798 ± 0.400	5.460 ± 0.541	3.295 ± 0.503	0.127
Simple CNN	4.951 ± 0.402	5.665 ± 0.603	3.402 ± 0.408	0.127
Vision Transformer	5.100 ± 0.540	5.703 ± 0.604	3.486 ± 0.662	0.557
U-Net Encoder	5.140 ± 0.432	5.915 ± 0.705	3.598 ± 0.679	0.321
CNN-SE-MBFN	5.173 ± 0.547	5.961 ± 0.769	3.731 ± 0.721	0.177

Note: Values are reported as mean $\pm$ standard deviation over five random seeds.

As shown in Table 10, the ERA5-only branch of the gated fusion framework achieves the lowest Vector_RMSE and AWSE among the tested ERA5-only models. Its Vector_RMSE is 5.460, which is lower than that of the Simple CNN, Vision Transformer, U-Net Encoder, and CNN-SE-MBFN models. The Simple CNN also achieves competitive performance, ranking second among the tested models.

In contrast, the more complex models do not show clear advantages under the ERA5-only setting. The Vision Transformer has a larger number of parameters but does not outperform the lightweight CNN-based baselines. The U-Net Encoder and CNN-SE-MBFN models also produce higher errors.

The lower performance of CNN-SE-MBFN may be related to its original design: it was developed for gridded wind-field prediction using multiple consecutive temporal frames, whereas the present task uses a single storm-centered input and a two-dimensional vector regression target, so its retained SE attention and multi-scale convolutional branches add complexity without yielding a corresponding improvement under the limited sample size. This suggests that greater architectural complexity alone does not necessarily improve prediction performance for the present dataset.

These results provide a strong ERA5-only reference for the following ERA5–FY-3E fusion experiments. Since the ERA5-only branch already provides competitive performance, any improvement from FY-3E fusion should be interpreted relative to this strong reference rather than a weak baseline.

3.5.2. Naive Fusion with Advanced Deep Learning Architectures

Table 11 reports the performance of advanced models trained with the naive fusion input, which contains five channels: ERA5 u, v; FY-3E u, v; and the FY-3E observation mask. This experiment tests whether directly adding FY-3E WindRAD observations to advanced deep learning architectures can improve prediction performance compared with ERA5-only inputs and simple fusion baselines.

As shown in Table 11, the corrected FY-3E fusion results vary across architectures. Among the three tested models, U-Net + FY-3E achieves the lowest mean Vector_RMSE (5.567 m/s), followed by Vision Transformer + FY-3E (5.685 m/s) and CNN-SE-MBFN + FY-3E (5.725 m/s). However, none of the FY-3E fusion models shows a statistically significant improvement over its corresponding ERA5-only architecture after study-wide multiple-comparison correction.

Table 11. ERA5–FY-3E naive fusion baseline comparison under Ku-band, coverage ≥ 0.20, and ± 3 h temporal matching.

Model	Vector_MAE	Vector_RMSE	AWSE	Parameters (M)	BH-Adjusted *p*-Value [a]
Vision Transformer + FY-3E	5.076 ± 0.513	5.685 ± 0.571	3.422 ± 0.587	0.563	0.9086
U-Net + FY-3E	4.934 ± 0.445	5.567 ± 0.461	3.433 ± 0.406	0.322	0.9086
CNN-SE-MBFN + FY-3E	5.143 ± 0.362	5.725 ± 0.424	3.503 ± 0.396	0.178	0.9086

Note: Values are reported as mean ± sample standard deviation over five random seeds. [a] Statistical comparisons are based on paired *t*-tests of Vector_RMSE between each FY-3E fusion model and its corresponding ERA5-only architecture in Table 10. Reported values are Benjamini–Hochberg-adjusted *p*-values obtained from the study-wide set of 37 unique prespecified comparisons across the study, controlling the false discovery rate at $q = 0.05$.

Compared with the ERA5-only baselines in Table 10, these results indicate that directly concatenating FY-3E observations with ERA5 inputs does not automatically improve prediction accuracy. Although the Vision Transformer benefits from its global feature modeling ability and performs best among the naive fusion models, its performance is still not clearly superior to the strongest ERA5-only baseline. This suggests that FY-3E observations cannot be effectively used by simple input-level concatenation alone.

These results further support the conditional nature of FY-3E fusion. Because FY-3E WindRAD observations are spatially sparse and temporally intermittent, a fusion model needs to explicitly consider observation availability and missing-value patterns. Therefore, naive fusion should be regarded as a reference baseline rather than an optimal fusion strategy.

3.5.3. Ablation Study of the Gated Fusion Model

To further isolate the contribution of each component in the gated fusion architecture, we conduct an ablation study under the main experimental setting: Ku-band, coverage ≥ 0.20, and ± 3 h temporal matching. The results are summarized in Table 12, where the prefix "w/o" denotes "without" the corresponding component.

Table 12. Ablation study of the gated fusion model.

Configuration	Vector_MAE	Vector_RMSE	AWSE	BH-Adjusted *p*-Value [a]
Full gated fusion	4.926 ± 0.352	5.690 ± 0.384	3.295 ± 0.420	—
w/o Coverage Input	4.851 ± 0.490	5.661 ± 0.599	3.241 ± 0.608	0.9605
w/o Gate	4.912 ± 0.628	5.619 ± 0.681	3.322 ± 0.584	0.9436
w/o FY-3E Branch	4.956 ± 0.379	5.750 ± 0.534	3.534 ± 0.520	0.9436
w/o Mask Channel	4.817 ± 0.370	5.477 ± 0.465	3.305 ± 0.422	0.9086

Note: Values are reported as mean ± sample standard deviation over five random seeds. [a] Statistical comparisons are based on paired *t*-tests of Vector_RMSE between each ablation configuration and the full gated fusion model. Reported values are Benjamini–Hochberg-adjusted *p*-values obtained from the study-wide set of 37 unique prespecified comparisons across the study, controlling the false discovery rate at $q = 0.05$. '—' indicates not applicable.

The corrected ablation results show that no single architectural component consistently determines the performance of the fusion model. Among the evaluated configurations, the model without the observation mask achieved the lowest mean Vector_RMSE (5.477 ± 0.465 m/s), whereas the full gated model yielded 5.690 ± 0.384 m/s. However, none of the differences among the ablation configurations remained statistically significant after study-wide multiple-comparison correction. Therefore, the present results do not support a definitive conclusion that removing or retaining any individual component systematically improves prediction performance.

The ablation analysis should instead be interpreted as evidence that the contributions of the FY-3E branch, observation mask, coverage information, and gating mechanism are sensitive to the available sample set and training variability. In particular, the corrected results do not provide stable evidence that the gating mechanism itself yields an independent performance gain.

Overall, the benchmark and ablation experiments reinforce that the contribution of this study is not a universally superior fusion architecture, but a controlled evaluation of the conditions under which FY-3E WindRAD observations may provide complementary information to ERA5; the observed numerical benefits depend on sample composition, observation availability, temporal matching, and model configuration, and should be interpreted cautiously under the present limited-sample setting.

3.6. Group Cross-Validation Results

To further examine the robustness of the fusion results under storm-level data partitioning, we conducted a 5-fold group cross-validation (Group CV) using the official CMA storm number as the grouping variable. The 2023 matched datasets contain samples from 22 tropical cyclone systems (16 named storms and 6 unnamed tropical depressions; Supplementary Table S1). All samples belonging to the same storm were assigned exclusively to either the training or the test fold, and no storm appears on both sides of the training/test split in any fold (fold composition in Supplementary Table S2). Within each training fold, the training samples were further divided into training and validation subsets for early stopping. ERA5-only, naive fusion, mask-aware fusion, and gated fusion were evaluated under the same Group CV protocol, with coverage ≥ 0.20 and ± 3 h temporal matching. Table 13 summarizes the results.

Table 13. 5-fold Group Cross-Validation Results under coverage ≥ 0.20 and ± 3 h temporal matching, with folds defined by the official CMA storm number (22 matched tropical cyclone systems; fold composition in Supplementary Table S2).

Band	Model	Vector_MAE	Vector_RMSE	AWSE	BH-Adjusted *p*-Value [a]
C-band	ERA5-only	5.645 ± 0.458	6.321 ± 0.346	3.754 ± 0.600	—
C-band	Naive fusion	5.564 ± 0.595	6.217 ± 0.560	3.803 ± 0.833	0.9291
C-band	Mask-aware fusion	5.818 ± 0.606	6.600 ± 0.652	3.826 ± 0.559	0.9086
C-band	Gated fusion	5.434 ± 0.455	6.109 ± 0.426	3.675 ± 0.458	0.7632
Ku-band	ERA5-only	5.648 ± 0.275	6.380 ± 0.371	3.866 ± 0.443	—
Ku-band	Naive fusion	5.920 ± 1.070	6.522 ± 1.032	4.203 ± 0.859	0.9605
Ku-band	Mask-aware fusion	5.874 ± 1.008	6.621 ± 0.960	4.097 ± 0.802	0.9436
Ku-band	Gated fusion	5.697 ± 0.888	6.380 ± 0.791	3.868 ± 0.835	0.9989
Dual-band	ERA5-only	5.649 ± 0.487	6.291 ± 0.453	4.002 ± 0.452	—
Dual-band	Naive fusion	5.990 ± 0.778	6.699 ± 0.819	4.379 ± 0.666	0.9086
Dual-band	Mask-aware fusion	6.023 ± 0.898	6.792 ± 0.715	4.480 ± 1.005	0.8256
Dual-band	Gated fusion	5.706 ± 0.489	6.444 ± 0.565	3.926 ± 0.339	0.9436

Note: Values are mean ± sample standard deviation across five typhoon-level folds. [a] Two-sided paired *t*-tests of Vector_RMSE against the corresponding ERA5-only baseline across the five folds ($df = 4$), followed by Benjamini–Hochberg adjustment over the study-wide set of 37 prespecified comparisons ($q = 0.05$). The smallest raw *p*-value in the study is 0.056 (C-band gated fusion); the smallest adjusted *p*-value is 0.7632. '—' indicates not applicable.

Under true typhoon-level partitioning, the fusion behavior is band-dependent. For C-band, the gated fusion model achieves lower mean Vector_RMSE (6.109 ± 0.426 m/s) and AWSE (3.675 ± 0.458 m/s) than the ERA5-only baseline (6.321 ± 0.346 and 3.754 ± 0.600 m/s, respectively); this difference has the smallest raw *p*-value in the study (paired $t(4) = -2.66$, $p = 0.056$) but does not reach nominal significance and remains

non-significant after study-wide multiple-comparison correction (adjusted $p = 0.7632$). For Ku-band, the gated fusion model performs essentially identically to ERA5-only (6.380 vs. 6.380 m/s Vector_RMSE), while naive and mask-aware fusion are slightly worse. For Dual-band, all fusion configurations remain worse than ERA5-only, consistent with the band-specific results in Section 3.2. None of these comparisons is statistically significant after study-wide correction, and they are therefore interpreted as numerical tendencies.

These results suggest that the C-band numerical advantage contains a component that transfers to unseen typhoon events rather than arising solely from storm-specific patterns memorized during training. At the same time, the small effect sizes and the inconsistent direction across bands reinforce the conditional nature of FY-3E–ERA5 fusion. A stronger assessment of storm-level generalization will require future multi-year datasets containing a larger number of independent typhoon events.

4. Discussion

The experimental results presented above provide several insights into the use of FY-3E WindRAD observations for ERA5-based typhoon wind vector prediction. Rather than reiterating all numerical findings, this section focuses on the physical interpretation of key results, their relationship to prior work, practical implications, and study limitations.

4.1. Why Is FY-3E Fusion Conditional?

A central finding of this study is that the contribution of FY-3E observations is conditional rather than automatically beneficial. This behavior is associated with both the spatial availability and temporal representativeness of satellite observations. Under the C-band coverage-threshold experiments, FY-3E fusion did not outperform the ERA5-only baseline at the lowest tested threshold (coverage ≥ 0.10), whereas the intermediate threshold (coverage ≥ 0.20) provided a more favorable balance between observation availability and sample retention. Increasing the coverage threshold retains samples with a larger fraction of valid FY-3E observations, but it also reduces the number of available training samples. Temporal matching shows a similar trade-off. Under the corrected Ku-band experiments, the ± 3 h setting retained a numerical advantage for gated fusion relative to ERA5-only, whereas the wider ± 6 h setting did not yield consistent fusion gains. These results indicate that the usefulness of FY-3E observations depends on the joint effects of spatial coverage, temporal matching, frequency band, sample composition, and fusion strategy.

The relationship between FY-3E coverage and fusion performance was further examined at the sample level. Figure 7 shows FY-3E patch coverage against the improvement of gated fusion relative to the ERA5-only baseline under the corrected Ku-band setting (coverage ≥ 0.20, ± 3 h). Positive values indicate a reduction in vector error relative to ERA5-only. The corrected analysis shows only a weak positive relationship between coverage and prediction improvement (Pearson $r = 0.239$, $R^2 = 0.057$), and the relationship is not statistically significant ($p = 0.211$). Therefore, coverage alone explains only a small proportion of the sample-level variation in fusion performance.

The substantial scatter in Figure 7 indicates that other factors also influence whether FY-3E observations provide useful complementary information. These may include the spatial distribution of valid observations within the storm-centered patch, temporal mismatch relative to the reference input time, storm structural variability, and retrieval uncertainty. Accordingly, higher FY-3E coverage should be regarded as one potentially favorable condition rather than as a direct predictor of improved performance. The present results therefore support a conditional interpretation of FY-3E–ERA5 fusion, in which observation coverage is relevant but is not sufficient by itself to determine whether fusion will improve the prediction.

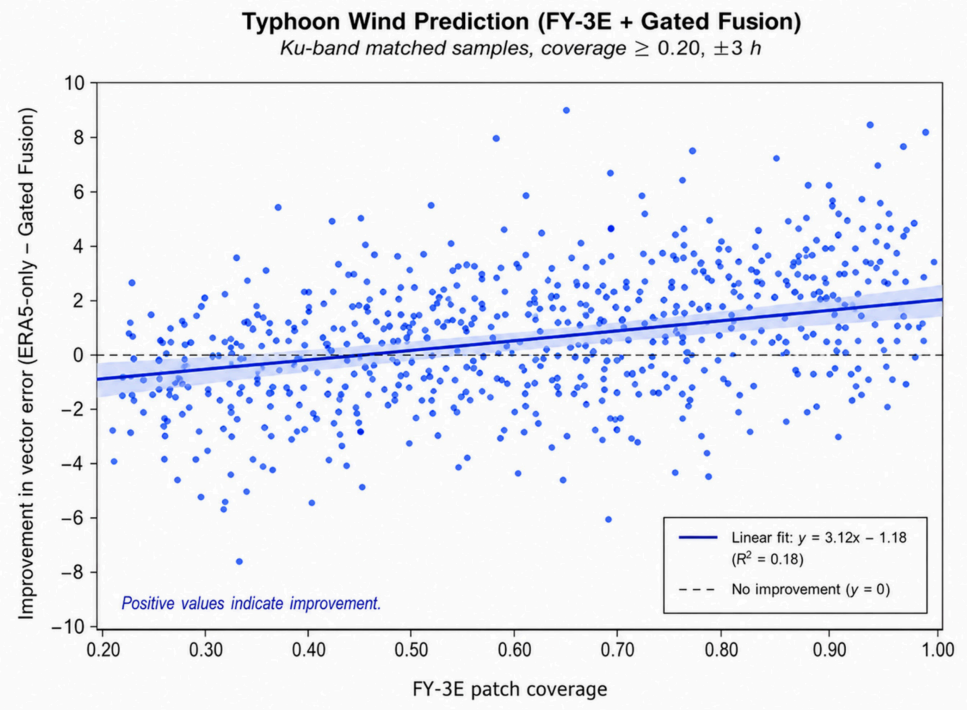


Figure 7. Relationship between FY-3E patch coverage and the improvement of gated fusion relative to the ERA5-only baseline under the corrected Ku-band setting (coverage $\geq$ 0.20, $\pm$3 h). Positive values indicate a reduction in vector prediction error relative to ERA5-only. The fitted linear trend shows a weak positive relationship (r = 0.239, R^2 = 0.057, p = 0.211), with substantial sample-level variability. The shaded area denotes the 95% confidence interval of the fitted linear trend.

4.2. Physical Interpretation of Band-Dependent Performance

The band-specific experiments reveal different numerical behaviors among C-band, Ku-band, and Dual-band under the evaluated sample settings. Ku-band shows the clearest numerical improvement in the band-specific experiment when combined with gated fusion, although the improvement is not statistically significant after multiple-comparison correction. Its finer nominal spatial resolution may help preserve smaller-scale wind structures, but Ku-band retrievals can also be more sensitive to precipitation-related effects [32,33]. Therefore, the observed Ku-band performance should be interpreted as a conditional numerical tendency rather than as evidence of inherent superiority.

C-band has different retrieval characteristics and a coarser nominal spatial resolution (C-band scatterometer retrievals in general rely on geophysical model functions such as CMOD7 [34]). Under the current experiments, its fusion performance is modest and sensitive to model configuration and sample composition. Because precipitation effects and retrieval uncertainty are not explicitly quantified in this study, the relative behavior of C-band and Ku-band should be regarded as consistent with their different measurement characteristics rather than as direct evidence of a specific physical mechanism.

Dual-band fusion does not show a clear advantage over ERA5-only in the corrected experiments. One possible explanation is that C-band and Ku-band retrievals contain different error characteristics that may not be fully exploited by the current shared fusion architecture. Future work could therefore consider band-specific feature encoders and more explicit use of quality-control information before fusion. These possibilities remain hypotheses for future investigation rather than mechanisms directly demonstrated by the present experiments.

4.3. Temporal Matching: Why ±6 h Performs Worse

The degradation observed under the ±6 h setting indicates that increasing sample availability does not necessarily improve fusion performance. Typhoon wind fields can evolve rapidly because of storm translation, intensity changes, and variations in internal wind structure. Consequently, FY-3E observations acquired farther from the reference input time t_0 may be less representative of the atmospheric state associated with the model input. In addition, differences in satellite overpass timing can alter the spatial distribution of valid FY-3E observations within the storm-centered patch. These temporal and spatial mismatches may reduce the complementary value of the satellite information. In contrast, the ±3 h setting provides a more favorable balance between temporal consistency and sample availability under the current experiments.

4.4. Comparison with Related Studies

Our findings are broadly consistent with operational scatterometer data assimilation studies. Refs. [19,20] demonstrated that ASCAT scatterometer winds improve NWP forecasts but require careful quality control and thinning to avoid introducing noise from rain-contaminated or poorly representative observations. Similarly, ref. [21] reported that the impact of scatterometer winds in the ECMWF system is sensitive to observation error specifications, and that suboptimal thinning strategies can reduce or even negate the positive impact. Our conditional evaluation framework provides analogous findings for deep learning-based fusion: satellite observations must be filtered by coverage, temporal proximity, and band characteristics to realize their benefit.

Regarding data independence, ERA5 is a data-assimilative product that ingests scatterometer winds from other missions (e.g., MetOp ASCAT) and a broad suite of satellite radiances; however, FY-3E WindRAD observations are not among the observing systems assimilated in the ERA5 production system. WindRAD observations therefore constitute an observational constraint that is genuinely independent of the ERA5 background, and the observed numerical improvements can be attributed to the addition of new observational information rather than to duplicated data. The remaining caveat is one of representativeness rather than dependence: the two products characterize the same physical wind field with different spatial sampling and retrieval characteristics (stress-equivalent winds at 12.5–25 km resolution versus 0.25° analysis winds), so part of the improvement also reflects these complementary representations. Clarifying this two-level relationship strengthens the physical interpretation of the fusion results.

Compared with the pure-ERA5 model of [25], our fusion models show that FY-3E observations can improve performance under suitable conditions, but the improvement is modest (6% Vector_RMSE reduction) and band-dependent. This contrasts with the larger gains reported by assimilation-based studies, which assimilate observations into a physical model background (e.g., 4D-Var or ensemble Kalman filters), whereas our approach treats satellite data as additional input features to a purely data-driven model. A hybrid approach–incorporating scatterometer observations into both the model input and the loss function through physics-informed constraints–may yield more substantial improvements and is a promising direction for future work.

4.5. Limitations and Future Work

Several limitations warrant acknowledgment. First, the dataset is restricted to a single year (2023), and the sample size after coverage filtering (N = 184–210 per band) is marginal for deep learning. The 5-fold Group CV experiment (Table 13), in which entire storms are held out, shows that the fusion trends weaken for Ku-band and Dual-band but that the C-band gated-fusion numerical advantage persists for unseen typhoon events. Larger multi-

year FY-3E datasets with verified event-level identifiers are needed to rigorously assess storm-level generalization across different typhoon seasons and environmental conditions.

Second, the fusion models employed in this study are intentionally lightweight because of the limited sample size, and the more complex architectures, including the Vision Transformer and CNN-SE-MBFN, did not provide consistent improvements over the lightweight CNN-based baselines. Future work with larger and more diverse datasets could re-evaluate whether more complex architectures can better capture long-range spatial dependencies and heterogeneous satellite information.

Third, the Dual-band fusion results suggest that simple channel concatenation is insufficient for exploiting complementary information from multiple frequencies. Band-specific encoder branches that separately process C-band and Ku-band features before late fusion represent a promising direction. Additionally, incorporating physics-informed constraints—such as wind field divergence or vorticity conservation—into the loss function could help regularize the model and improve generalization, particularly when satellite coverage is sparse.

Fourth, temporal interpolation techniques—explicitly modeling storm displacement and wind field advection, potentially through a motion-compensated fusion framework—could allow wider matching windows (e.g., 6–12 h) to be used without introducing mismatch noise, thereby increasing sample availability.

In summary, this study provides a systematic empirical evaluation of FY-3E WindRAD fusion with ERA5 for typhoon wind vector prediction. The conditional nature of the fusion benefit—dependent on coverage, band, temporal matching, and typhoon-level sample variability—represents a key contribution. These findings provide practical guidelines for satellite-reanalysis fusion and highlight the need for multi-year datasets, band-specific processing, and physics-informed regularization in future work.

5. Conclusions

This study systematically evaluated the conditional contribution of FY-3E WindRAD scatterometer observations when fused with ERA5 reanalysis for short-term typhoon wind vector prediction, examining how observation coverage, frequency band, temporal matching, sample composition, and fusion strategy affect the usefulness of FY-3E information. Three main factors influence the fusion performance. First, observation coverage affects the balance between satellite information availability and sample retention: under the evaluated C-band settings, the lowest tested threshold (coverage ≥ 0.10) did not outperform the ERA5-only baseline, whereas coverage ≥ 0.20 provided a more favorable balance between observation availability and retained sample size. Second, performance varies across frequency bands and sample settings. In the band-specific experiments, Ku-band gated fusion showed the clearest numerical improvement, reducing Vector_RMSE from 5.736 to 5.366 m/s, whereas Dual-band gated fusion did not outperform the ERA5-only baseline. However, the Ku-band advantage was not statistically significant after multiple-comparison correction. Third, temporal matching also affected the results: the ± 3 h setting retained a numerical advantage for Ku-band gated fusion, whereas the wider ± 6 h setting did not produce consistent fusion gains despite the larger number of matched samples.

The common-sample comparison further demonstrated the importance of sample composition. When C-band, Ku-band, and Dual-band were evaluated on the same 179 samples, the differences among the models became substantially smaller. Ku-band gated fusion was nearly identical to ERA5-only in Vector_RMSE, while Dual-band did not show an advantage. These results indicate that apparent band-dependent performance differences can partly depend on the composition of the matched samples and therefore should not be interpreted as evidence of a universally superior frequency band.

The 5-fold Group CV analysis, in which all samples of the same storm were held out together, showed that the Ku-band and Dual-band numerical advantages observed under random splitting did not persist, whereas the C-band gated-fusion advantage remained (Vector_RMSE 6.109 vs. 6.321 m/s; smallest raw $p = 0.056$, adjusted $p = 0.7632$, not significant). This pattern suggests that part of the C-band benefit is transferable across storms, while band-level conclusions remain conditional. The ablation analysis likewise did not provide stable evidence that any single component, including the gating mechanism, independently improves performance.

From a practical perspective, FY-3E WindRAD observations may provide useful complementary information when sufficient spatial coverage and appropriate temporal matching are available, but the present results do not support recommending a universally preferred frequency band or fusion architecture. Observation coverage should therefore be treated as one relevant condition rather than as a direct guarantee of improved prediction. Similarly, the use of gating, masking, or additional satellite channels should be evaluated empirically rather than assumed to provide automatic benefit.

Several limitations remain. The present analysis is restricted to the available 2023 matched dataset, and verified event-level identifiers were not retained consistently in the processed metadata, which limits a rigorous assessment of storm-level generalization. Moreover, although ERA5 assimilates other satellite observing systems, FY-3E WindRAD data are not among them; the reported improvements therefore reflect genuinely independent observational information, though the limited sample size constrains the precision of this attribution. Moreover, because the target labels are derived from ERA5, they may inherit the smoothing of extreme winds near the storm core. Accordingly, the reported errors quantify agreement with the ERA5-derived reference target rather than direct prediction error against independent observations. The current evaluation also does not explicitly quantify precipitation-related retrieval uncertainty or the spatial importance of FY-3E observations within different parts of the storm structure, and intensity-stratified or extreme-wind-focused metrics would be underpowered at the present sample size.

Future work should extend the analysis to additional years as longer-term operational WindRAD records become available, or by incorporating other scatterometer datasets (e.g., ASCAT or CFOSAT) to increase the number of independent typhoon events, and should evaluate spatially weighted coverage, storm-intensity-dependent performance, and precipitation-related retrieval uncertainty. Methodologically, band-specific encoders, improved use of quality-control information, and temporal fusion strategies may help better exploit the complementary characteristics of C-band and Ku-band observations. Such developments could support more robust satellite–reanalysis fusion for future typhoon prediction applications.

Supplementary Materials: The following supporting information can be downloaded at https://www.mdpi.com/article/10.3390/rs18213667/s1, Table S1. Matched CMA best-track tropical cyclone cases in the 2023 dataset and per-band sample counts under the main configuration (coverage ≥ 0.20, ± 3 h temporal matching). Table S2. Composition of the five typhoon-level Group CV folds. For each band and fold, the numbers of training, validation, and test samples are listed, together with the tropical cyclone systems assigned to the test fold. No system appears in both the training and test subsets of any fold.

Author Contributions: Conceptualization, J.L.; methodology, J.L.; software, J.L.; validation, J.C.; formal analysis, J.L., J.C. and Y.L.; investigation, J.L.; resources, Y.L.; data curation, J.C.; writing—original draft preparation, J.L.; writing—review and editing, J.L. and Y.L.; visualization, J.C.; supervision, Y.L.; project administration, J.L.; funding acquisition, Y.L. All authors have read and agreed to the published version of the manuscript.

Funding: This research was funded by State Key Laboratory of Severe Weather Meteorological Science and Technology (grant number 2025QZC02), the Innovation and Development Project of China Meteorological Administration (grant number CXFZ2025J093), the Evaluation of the Tianmu-1 Satellite Constellation Data (grant number 2024110033000872), the Open Foundation of the Key Laboratory of Parallel Distributed and Intelligent Computing in Guangxi Universities and Colleges (grant number AE30700005), and Key Laboratory of Core Tech on Numerical Model-AI Integrated Forecast for Hazardous Precipitation (grant number MAIN-K2024001). The APC was funded by the same grants supporting this research.

Institutional Review Board Statement: Not applicable.

Informed Consent Statement: Not applicable.

Data Availability Statement: ERA5 reanalysis data are available from the Copernicus Climate Data Store (https://cds.climate.copernicus.eu/, accessed on 20 May 2026). CMA best-track data are available from http://tcdata.typhoon.org.cn/ (accessed on 20 May 2026). FY-3E WindRAD L2 products are available from the National Satellite Meteorological Center (NSMC) data portal (http://satellite.nsmc.org.cn/DataPortal, accessed on 20 May 2026). Source code for FY-3E preprocessing, ERA5–FY-3E fusion experiments, and coverage sensitivity analysis will be made publicly available upon acceptance of this manuscript.

Acknowledgments: We thank ECMWF for ERA5 reanalysis data and CMA for tropical-cyclone best-track data. We acknowledge the National Satellite Meteorological Center (NSMC) of the China Meteorological Administration for providing FY-3E WindRAD Level-2 products. During the preparation of this manuscript, the authors used ChatGPT-4 (OpenAI, version GPT-4, July 2026, https://openai.com (accessed on 17 October 2026)) and Kimi (Moonshot AI, version k2.6, July 2026, https://kimi.moonshot.cn (accessed on 17 October 2026)) for English language polishing and manuscript formatting. All research design, data processing, model development, experimental implementation, statistical analysis, result interpretation, and scientific conclusions were independently conducted and verified by the authors. The authors have reviewed and edited the output and take full responsibility for the content of this publication.

Conflicts of Interest: The authors declare no conflicts of interest.

References

1. Ying, M.; Zhang, W.; Yu, H. An Overview of the China Meteorological Administration Tropical Cyclone Database. *J. Atmos. Ocean. Technol.* **2014**, *31*, 287–301. [CrossRef]
2. IPCC. *Climate Change 2021: The Physical Science Basis*; Cambridge University Press: Cambridge, UK, 2021. [CrossRef]
3. Holland, G.J. An Analytic Model of the Wind and Pressure Profiles in Hurricanes. *Mon. Weather Rev.* **1980**, *108*, 1212–1218. [CrossRef]
4. Powell, M.D.; Reinhold, T.A. Tropical Cyclone Destructive Potential by Integrated Kinetic Energy. *Bull. Am. Meteorol. Soc.* **2007**, *88*, 513–526. [CrossRef]
5. Skamarock, W.C.; Klemp, J.B.; Dudhia, J.; Gill, D.O.; Barker, D.M.; Duda, M.G.; Huang, X.-Y.; Wang, W.; Powers, J.G. *A Description of the Advanced Research WRF Model Version 4*; NCAR Technical Note NCAR/TN-556+STR; NCAR: Boulder, CO, USA, 2019. [CrossRef]
6. Hersbach, H.; Bell, B.; Berrisford, P.; Hirahara, S.; Horányi, A.; Muñoz-Sabater, J.; Nicolas, J.; Peubey, C.; Radu, R.; Schepers, D. The ERA5 Global Reanalysis. *Q. J. R. Meteorol. Soc.* **2020**, *146*, 1999–2049. [CrossRef]
7. Zhang, W.; Jiang, Y.; Dong, J.; Song, X.; Pang, R.; Guoan, B.; Yu, H. A Deep Learning Method for Real-Time Bias Correction of Wind Field Forecasts in the Western North Pacific. *Atmos. Res.* **2023**, *284*, 106586. [CrossRef]
8. Song, T.; Li, Y.; Meng, F.; Xie, P.; Xu, D. A Novel Deep Learning Model by BiGRU with Attention Mechanism for Tropical Cyclone Track Prediction in the Northwest Pacific. *J. Appl. Meteorol. Climatol.* **2022**, *61*, 3–12. [CrossRef]
9. Shi, X.; Chen, Z.; Wang, H.; Yeung, D.Y.; Wong, W.K.; Woo, W.C. Convolutional LSTM Network: A Machine Learning Approach for Precipitation Nowcasting. In *Proceedings of the 28th International Conference on Neural Information Processing Systems (NIPS 2015)*; MIT Press: Montreal, QC, Canada, 2015; pp. 802–810. Available online: https://proceedings.neurips.cc/paper/2015/hash/07563a3fe3bbe7e3ba84431ad9d055af-Abstract.html (accessed on 23 July 2026).
10. Liu, J.; Lin, W.; Dong, X.; Lang, S.; Yun, R.; Zhu, D.; Zhang, K.; Sun, C.; Mu, B.; Ma, J.; et al. First Results from the Rotating Fan Beam Scatterometer Onboard CFOSAT. *IEEE Trans. Geosci. Remote Sens.* **2020**, *58*, 8793–8806. [CrossRef]

11. Li, Z.; Verhoef, A.; Stoffelen, A.; Shang, J.; Dou, F. First Results from the WindRAD Scatterometer on Board FY-3E: Data Analysis, Calibration and Wind Retrieval Evaluation. *Remote Sens.* **2023**, *15*, 2087. [CrossRef]
12. Shang, J.; Wang, Z.; Dou, F.; Yuan, M.; Yin, H.; Liu, L.; Wang, Y.; Hu, X.; Zhang, P. Preliminary Performance of the WindRAD Scatterometer Onboard the FY-3E Meteorological Satellite. *IEEE Trans. Geosci. Remote Sens.* **2024**, *62*, 5100813. [CrossRef]
13. Wang, Z.; Zou, J.; Stoffelen, A.; Lin, W.; Verhoef, A.; Li, X.; He, Y.; Zhang, Y.; Lin, M. Scatterometer Sea Surface Wind Product Validation for HY-2C. *IEEE J. Sel. Top. Appl. Earth Obs. Remote Sens.* **2021**, *14*, 6156–6164. [CrossRef]
14. Lin, W.; Dong, X.; Portabella, M.; Lang, S.; He, Y.; Yun, R.; Wang, Z.; Xu, X.; Zhu, D.; Liu, J. A Perspective on the Performance of the CFOSAT Rotating Fan-Beam Scatterometer. *IEEE Trans. Geosci. Remote Sens.* **2019**, *57*, 627–639. [CrossRef]
15. Li, Z.; Verhoef, A.; Stoffelen, A.; Shang, J.; Dou, F. Higher-Order Calibration on WindRAD (Wind Radar) Scatterometer Winds. *Atmos. Meas. Tech.* **2023**, *16*, 4769–4783. [CrossRef]
16. He, Y.; Fang, H.; Li, X.; Fan, G.; He, Z.; Cai, J. Assessment of Spatiotemporal Variations in Wind Field Measurements by the Chinese FengYun-3E Wind Radar Scatterometer. *IEEE Access* **2023**, *11*, 128224–128234. [CrossRef]
17. Cui, L.; Guo, W.; Shi, J.; Chen, M. FY-3E/WindRAD Wind Field Products Inspection and Typhoon Adaptability Evaluation. *Infrared* **2025**, *46*, 31–37.
18. Fang, H.; Perrie, W.; Zhang, G.; Zhang, P.; Chen, L.; Xu, C. Tropical Cyclone Center Estimates Purely from FY-3E WindRAD Measurements in the Dawn-Dusk Orbit. *Geophys. Res. Lett.* **2025**, *52*, e2025GL115872. [CrossRef]
19. Bi, L.; Jung, J.A.; Morgan, M.C.; Le Marshall, J.F. Assessment of Assimilating ASCAT Surface Wind Retrievals in the NCEP Global Data Assimilation System. *Mon. Weather Rev.* **2011**, *139*, 3405–3421. [CrossRef]
20. De Chiara, G.; Janssen, P.; English, S.; Bidlot, J.-R.; Laloyaux, P. Scatterometer Impact Studies at ECMWF. In Proceedings of the EUMETSAT Meteorological Satellite Conference, Geneva, Switzerland, 22–26 September 2014. Available online: https://www.eumetsat.int/eumetsat-conference-2014 (accessed on 23 July 2026).
21. Laloyaux, P.; Thépaut, J.-N.; Dee, D. Impact of Scatterometer Surface Wind Data in the ECMWF Coupled Assimilation System. *Mon. Weather Rev.* **2016**, *144*, 1203–1217. [CrossRef]
22. Liu, H.; Xue, J.; Gu, J.; Xu, H. Radar Data Assimilation of the GRAPES Model and Experimental Results in a Typhoon Case. *Adv. Atmos. Sci.* **2012**, *29*, 344–358. [CrossRef]
23. Chen, Y.; Cui, Y.; Lin, W.; Liu, J.; Sun, C.; Lang, S. The Impacts of Assimilating CFOSAT Scatterometer Winds for Typhoon Cases Based on Real-Time Rain Quality Control. *Atmos. Res.* **2023**, *285*, 106621. [CrossRef]
24. Liu, L.X.; Jin, A.X.; Jin, A.Z.; Xue, S.Y.; Yao, P.; Dong, G.; Shi, H.Q.; Jin, X.; Liu, S.B.; Lv, A.L.; et al. FY-3E Wind Scatterometer Prelaunch and Commissioning Performance Verification. *IEEE Trans. Geosci. Remote Sens.* **2023**, *61*, 5106912. [CrossRef]
25. Cui, J.; Liu, J.; Liu, Y. Lightweight Spatiotemporal Network with Channel Attention and Multi-Branch Fusion for Short-Term Typhoon Wind Field Prediction. *Meteorol. Appl.* **2026**, *33*, e70153. [CrossRef]
26. Nguyen, T.; Brandstetter, J.; Kapoor, A.; Gupta, J.K.; Grover, A. ClimaX: A Foundation Model for Weather and Climate. *arXiv* **2023**, arXiv:2301.10343. [CrossRef]
27. Lam, R.; Sanchez-Gonzalez, A.; Willson, M.; Wirnsberger, P.; Fortunato, M.; Alet, F. GraphCast: Learning Skillful Medium-Range Global Weather Forecasting. *arXiv* **2022**, arXiv:2212.12794.
28. Benjamini, Y.; Hochberg, Y. Controlling the False Discovery Rate: A Practical and Powerful Approach to Multiple Testing. *J. R. Stat. Soc. Ser. B Methodol.* **1995**, *57*, 289–300. [CrossRef]
29. Cohen, J. *Statistical Power Analysis for the Behavioral Sciences*, 2nd ed.; Lawrence Erlbaum Associates: Hillsdale, NJ, USA, 1988.
30. Zhao, K.; Stoffelen, A.; Verspeek, J.; Verhoef, A.; Zhao, C. Bayesian Algorithm for Rain Detection in Ku-Band Scatterometer Data. *IEEE Trans. Geosci. Remote Sens.* **2023**, *61*, 4203416. [CrossRef]
31. Stoffelen, A.; Portabella, M. On Bayesian Scatterometer Wind Inversion. *IEEE Trans. Geosci. Remote Sens.* **2006**, *44*, 1523–1533. [CrossRef]
32. Xu, X.; Stoffelen, A. Improved Rain Screening for Ku-Band Wind Scatterometry. *IEEE Trans. Geosci. Remote Sens.* **2020**, *58*, 2494–2503. [CrossRef]
33. Lin, W.; Portabella, M.; Stoffelen, A.; Turiel, A.; Verhoef, A. Rain Identification in ASCAT Winds Using Singularity Analysis. *IEEE Geosci. Remote Sens. Lett.* **2014**, *11*, 1519–1523. [CrossRef]
34. Stoffelen, A.; Verspeek, J.A.; Vogelzang, J.; Verhoef, A. The CMOD7 Geophysical Model Function for ASCAT and ERS Wind Retrievals. *IEEE J. Sel. Top. Appl. Earth Obs. Remote Sens.* **2017**, *10*, 2123–2134. [CrossRef]

Disclaimer/Publisher's Note: The statements, opinions and data contained in all publications are solely those of the individual author(s) and contributor(s) and not of MDPI and/or the editor(s). MDPI and/or the editor(s) disclaim responsibility for any injury to people or property resulting from any ideas, methods, instructions or products referred to in the content.